~~Spatio-temporal synchronization~~ The role of ~~heavy rainfall eventstriggered by~~ atmospheric rivers in the distribution of heavy precipitation events over North America

Sara M. Vallejo-Bernal[1,2], Frederik Wolf[1], Niklas Boers[1,3,4], Dominik Traxl[1], Norbert Marwan[1,2], and Jürgen Kurths[1,2]

[1]Research Domain IV - Complexity Science, Potsdam Institute for Climate Impact Research (PIK) – Member of the Leibniz Association, Potsdam, Germany
[2]Institute of Geoscience, University of Potsdam, Germany
[3]Earth System Modelling, School of Engineering & Design, Technical University of Munich, Germany
[4]Global Systems Institute and Department of Mathematics, University of Exeter, UK

Correspondence: Sara M. Vallejo-Bernal (vallejo.bernal@pik-potsdam.de)

Abstract. Atmospheric rivers (ARs) are filaments of extensive water vapor transport in the lower troposphere, that play a crucial role in the distribution of fresh water, but can also cause natural and economical damage by facilitating heavy ~~rainfall~~precipitation. Here, we investigate the large-scale spatio-temporal synchronization patterns of heavy ~~rainfall~~ precipitation events (HPEs) over the western coast and the continental regions of North America (NA), during the period from 1979 to 2018. In particular, we utilize event synchronization and a complex network approach incorporating varying delays to examine the temporal evolution of spatial patterns of ~~heavy rainfall events~~ HPEs in the aftermath of land-falling ARs. For that, we employ the SIO-R1 catalog of ARs that ~~land-fall over~~ landfall on the western coast of NA, ~~categorized~~ ranked in terms of strength and persistence on an AR-intensity scale which varies from ~~category~~ level AR1 to AR5, along with daily ~~rainfall~~ precipitation estimates from the ERA5 reanalysis with $0.25°$ spatial resolution. Our analysis reveals a cascade of synchronized ~~heavy rainfall events~~HPEs, triggered by ARs of ~~category~~ level AR3 or higher: ~~in~~ on the first 3 days after ~~the first day of an AR strike, rainfall events~~ an AR makes landfall, HPEs mostly occur and synchronize along the western coast of NA. In the subsequent days, moisture can be transported to central and eastern Canada and cause synchronized but delayed ~~heavy rainfall~~ HPEs there. Furthermore, we assess the robustness of our findings by studying an additional AR detection method. Finally, analyzing the anomalies of integrated water vapor transport, geopotential height, upper-level meridional wind, and ~~rainfall~~precipitation, we find atmospheric circulation patterns that are consistent with the spatio-temporal evolution of the synchronized ~~heavy rainfall events~~HPEs. Understanding and revealing the effects of ARs in the ~~rainfall~~ precipitation patterns over NA will lead to ~~better anticipating the evolution of the climate dynamics of the region~~ a better understanding of inland HPEs and how changing climate dynamics may affect precipitation occurrence and consequent impacts in the context of a ~~changing climate~~warming atmosphere.

1 Introduction

Atmospheric rivers (ARs) are channels of enhanced water vapor flux that transport moisture over thousands of kilometres, often from the tropics to the mid-latitudes of both hemispheres, where they ~~land-fall and cause copious rainfall (e. g. (Zhu and Newell, 1998; Ralph and Dettinger, 2011; Baggett et al., 2017; Eiras-Barca et al., 2018; Mundhenk et al., 2018; **?**; Ralph et al., 2).~~ can cause substantial precipitation following landfall (e.g. Zhu and Newell, 1998; Ralph and Dettinger, 2011; Baggett et al., 2017; Eiras-. Located in the lower troposphere, ARs can persist from several hours to several days~~and~~ , carrying as much water as the Amazon river (Newell et al., 1992). Therefore, they play a crucial role in the global water cycle (Neiman et al., 2008), the Arctic water influx (Baggett et al., 2016), and ~~can cause heavy rainfall (Neiman et al., 2008; Krichak et al., 2015). Due to the increase of water vapor, it is to be expected that their frequency (Gao et al., 2015; Hagos et al., 2016) and intensity (Payne et al., 2020) will increase in the next decades in the context of ongoing climate change.~~

the occurrence of heavy precipitation events (HPEs) (Neiman et al., 2008; Krichak et al., 2015). However, intense and persistent ARs have also been associated with natural hazards such as extreme winds, floods, and landslides, and their respective economic losses (Ramseyer and Teale, 2021; Sharma and Déry, 2020; Corringham et al., 2019; Ralph et al., 2019; Waliser and Guan, 2017) . Further motivated by their high environmental, social and economical impacts, occurrences of ARs have been studied intensively in the last decade, especially on the western coasts of North America (NA) and ~~in Europe (Smith et al., 2010; Dettinger et al., 2011; N). ARs typically form at the front of a~~ Europe (Smith et al., 2010; Dettinger et al., 2011; Newman et al., 2012; Lavers and Villarini, 2013; W .

With this increased interest in understanding the dynamics, impacts and future evolution of ARs, a plethora of methodological approaches to identify and track these atmospheric features, both in space and time, has been proposed and multiple AR catalogs have been produced and made available to the public (Gershunov et al., 2017; Guan and Waliser, 2015; Prabhat et al., 2021; Pan a . This abundance of information has brought big challenges to the climate research community, as the climatological statistics of ARs have proven to be highly dependent on the identification method used (Huning et al., 2017), affecting in particular the resultant AR climatologies and the attribution of high-impact weather and climate events to ARs (Shields et al., 2018). As a collective effort to address these issues, the Atmospheric River Tracking Method Intercomparison Project (ARTMIP) has quantified and analyzed the uncertainties in AR science based on the choice of detection/tracking methodology (Shields et al., 2018; Rutz et . The results achieved by the scientific community involved provide nowadays the guidelines for choosing the most appropriate algorithm for a given scientific question or region of interest.

As a consequence, novel and relevant topics of AR science have been studied, such as the initiation and evolution of ARs and their moisture sources (Guan and Waliser, 2019; Waliser and Guan, 2017; Rutz et al., 2014), and the foreseen response of ARs to a warmer or different climate (Gao et al., 2015; Hagos et al., 2016; Payne et al., 2020). Thanks to these contributions, the following key findings have been recently revealed to the climate scientific community: *i)* in the northern hemisphere, ARs usually originate in the mid-latitude ~~cyclone and cause rainfall due to an ascent of air masses by a warm conveyor belt intersecting with orography (Zhang et al., 2019; Sharma and Déry, 2020). Given that ARs~~ocean basins (Guan and Waliser, 2019) paired with extratropical cyclones (Zhang et al., 2019). *ii)* As they travel east, ARs accumulate and transport moisture, primarily

to the western coasts of North America and Europe, where they facilitate precipitation and play a key role both in the fresh water supply and in the occurrence of HPEs. *iii)* In the context of ongoing climate change, a poleward shift of the land-falling ~~at the western coast of NA frequently accumulate their moisture over the central Pacific, and that the exact location of the cyclonic storms heavily influences the location of the AR, AR frequency and intensity are modulated by the Madden-Julian Oscillation (MJO), the Quasi-Biannual Oscillation (QBO) , the El-Niño Southern Oscillation (ENSO) and the Pacific Decadal Oscillation (PDO) (Baggett et al., 2017; Mundhenk et al., 2018; Zhou et al., 2021). Along the dryer southwestern coast of NA, ARs play an essential role in the water supply (Smith et al., 2010; Dettinger et al., 2011). There, the less intense ARs are beneficial and act as central sources of fresh water by facilitating rainfall, whereas intense ARs cause large natural and economical damage (Waliser and Guan, 2017; Corringham et al., 2019; Gershunov et al., 2019; Ralph et al., 2019)~~location, together with an increase in the frequency and intensity of ARs, can be expected in the coming decades as a response to the higher water vapor content in a warmer atmosphere (Gao et al., 2016; Hagos et al., 2016; Payne et al., 2020). Moreover, compared with the present, ARs affecting middle and high elevations are expected to result in more liquid than solid precipitation, exacerbating the potential risk and severe impacts of natural hazards such as floods and landslides (Mahoney et al., 2018).

~~Although~~ In light of the scientific knowledge that has been gained in recent decades about ARs, there has been an increasing effort in characterizing and predicting ~~AR strikes~~ the landfall of ARs along the North American west coast by presenting comprehensive analyses of their drivers and properties~~of AR-related land-fall~~. However, the spatio-temporal synchronization patterns of heavy ~~rainfall~~ precipitation events (HPEs) induced by ARs have not yet been studied. Here, we understand spatio-temporal synchronization as a relation between ~~time series~~ pairs of precipitation time series measured at different locations, ~~where~~ for which events in one time series ~~measured at a location~~ are significantly followed or preceded by events ~~at another~~in the other one. Such an assessment has led, among other findings ~~(see e.g. (Boers et al., 2013; Stolbova et al., 2014; Agarwal et al., 2019; We)~~(see e.g. Boers et al., 2013; Stolbova et al., 2014; Agarwal et al., 2019; Wolf et al., 2020b), to forecasting ~~rainfall~~ precipitation events in the Eastern Central Andes (Boers et al., 2014a) and identifying Rossby waves as one controlling mechanism of ~~heavy rainfall~~ HPEs worldwide (Boers et al., 2019). In this light, it has not been examined to what extent ARs are accompanied by characteristic synchronization patterns of ~~heavy rainfall~~HPEs. Additionally, ~~we study~~ the lag-dependent spatial impact of ARs ~~hitting~~ making landfall on the western coast ~~. We utilize two different catalogs with different AR-tracking schemes to address these specific research questions and to~~ of NA remains unrevealed. To elaborate on the issues explained and examined by the ARTMIP project ~~(?Rutz et al., 2019; O'Brien et al., 2022), which showed that observations are often catalog-dependent~~(Shields et al., 2018; Rutz et al., 2019; O'Brien et al., 2022), in this study we address these specific research questions using two different catalogs with different AR-tracking schemes. Both catalogs considered here, the SIO-R1 product which was recently published by Gershunov et al. (2017) and a self-constructed one which is based on the IPART algorithm ~~Xu et al. (2020)~~Xu et al. (2020); Traxl (2022), cover the period between 1979 and 2018. Based on the occurrence of ARs, we perform time series and complex network analyses evaluating the spatio-temporal correlation of ~~heavy rainfall events~~ HPEs and their relation to ARs. To interpret our results, we furthermore study the corresponding climatologies of different variables such as ~~upper-level meridional~~ wind and geopotential height at 500 hPa.

The paper is structured as follows: first, we introduce the employed data sets and methods, in particular the characteristics of the two AR catalogs, the ERA5 reanalysis and the event synchronization (ES) and complex network techniques. Second, we conduct an ES-based assessment of the temporal correlation between ~~AR strikes and heavy rainfall events~~ land-falling ARs and HPEs for different lags. Having revealed different temporal scales at which AR-related ~~heavy rainfall events~~ HPEs occur, we set up two climate networks based on ~~rainfall events~~ HPEs taking place at different lags. Finally, we study ~~composites~~ composite anomalies of integrated water vapor transport, geopotential height, ~~upper-level meridional~~ wind, and ~~rainfall~~ precipitation for the times during which we identified features of synchronized ~~heavy rainfall~~ HPEs and we discuss our findings in the context of the guiding climatology.

2 Data and Methods

2.1 Data sets

For our analyses, we utilize data from the ERA5 reanalysis ~~(ECMWF, 2021)~~(Hersbach et al., 2020; ECMWF, 2021). All ERA5 data sets are available on a longitude-latitude grid with a spatial resolution of $0.25° \times 0.25°$. We construct daily estimates for integrated water vapor transport (IVT), geopotential height at 500 hPa, ~~meridional wind at 250~~wind at 650 hPa, and ~~rainfall~~ precipitation by considering the daily mean of the hourly data sets for the period between 1979 and 2018.

To examine the synchronization of ~~heavy rainfall~~HPEs, we especially consider the 95^{th} percentile thresholds of the daily precipitation estimates. Only days exceeding 1 mm of total ~~rainfall~~ precipitation, which we refer to as *wet days*, are used for computing the percentiles.

Recent studies have revealed the biases present in the ERA5 reanalysis, especially for precipitation estimations. Disagreements on the number of wet days, the co-occurrence of precipitation events and the precipitation intensity were identified, along with a consistent pattern of decreasing agreement with increasing intensity of events, independently of the season (Rivoire et al., 2021) . Larger differences were found over western NA, were ERA5 has additional difficulties in detecting and estimating orographic precipitation events (Adhikari and Behrangi, 2022). However, and despite of these biases, we use ERA5 estimates for our analyses to maintain the consistency between the variables and their agreement with the large-scale circulation patterns.

In addition to the ERA5 reanalysis data set, we use the SIO-R1 catalog of ARs by Gershunov et al. (2017). It includes ARs land-falling ~~at~~ on the western coast of NA and was constructed using Lagrangian backtracking of high values of two variables, namely the vertically integrated horizontal vapor transport (IVT), and the vertically integrated water vapor (IWV), on a longitude-latitude grid with a resolution of $2.5° \times 2.5°$. The catalog features a 6-hourly time series indicating whether an AR has been active, the grid cells covered by the AR, and the IVT over the grid cell along the coast where the AR ~~land-falls~~made landfall. We transform the 6-hourly catalog into a daily one by considering each day with at least one (of the four) 6-hourly time ~~steps with an AR present~~ step with an active AR as an *AR-day*. Approximately one-third of all days of the ~~considered~~ analysis period are AR-days (at least one AR active somewhere in the spatial domain covered by the catalog). These days are distributed relatively equally over the different years but are strongly seasonally clustered in the boreal autumn and winter.

Furthermore, we create an additional catalog of ARs with features similar to the SIO-R1 catalog but using the Image-Processing-based Atmospheric River Tracking (IPART) algorithm (Xu et al., 2020). As opposed to conventional detection methods that rely on thresholding of IVT and/or IWV fields (for instance the detection algorithm of the SIO-R1 catalog), IPART implements the detection task from a spatio-temporal scale perspective and is, therefore, free from magnitude thresholds. The advantage of IPART's approach is that it negates the implicit assumption of thresholding approaches that the atmospheric moisture level stays unchanged throughout the analysis period. As input to the IPART algorithm, we use IVT-fields of the ERA5 reanalysis data set re-gridded to a spatial resolution of $0.75° \times 0.75°$ and a temporal resolution of 6 hours. The parameters passed to the different steps of the IPART algorithm are summarized in Table A1 in appendix A (Traxl, 2022). We transform the 6-hourly product into a daily one in the same manner as described for the SIO-R1 catalog.

2.2 ~~Event Synchronization (ES)~~

To separate the impact of rather weak ARs from strong ARs, we rank AR events of both catalogs in terms of strength and persistence on the AR-intensity scale proposed by Ralph et al. (2019) and using the notation in Eiras-Barca et al. (2021). As a result, each AR event is assigned a level that increases from AR1 to AR5 and we run our analysis repeatedly, excluding ARs from lower levels.

2.2 Event Synchronization (ES) between land-falling ARs and HPEs

Event synchronization (ES), as initially introduced by Quiroga et al. (2002), is a ~~method to quantify the synchronization~~ temporal correlation measure that quantifies the co-variability of events in a pair of time series. While ~~ES~~ it has been originally proposed for analyzing spike trains in electroencephalographic time series, ES is nowadays an established tool employed to construct ~~functional~~ climate networks (Malik et al., 2012; Boers et al., 2013, 2019; Ozturk et al., 2019; Wolf et al., 2020a).

~~Using ES, two events~~ To define ES, let the sequence $\{t_l^\mu\}_{\mu=1,\dots,n_l}$ denote the time series of ARs of level l ~~and m in time series describing observations made at locations~~ or higher, making landfall at the western coast of NA, and let the sequence $\{t_i^\nu\}_{\nu=1,\dots,n_i}$ denote the time series of HPEs observed at grid cell i. The total number of land-falling ARs of level l or higher and the total number of HPEs at grid cell i are denoted by n_l and ~~j at times t_l^i and t_m^j are considered~~ n_i respectively. We say that the HPE ν, observed at location i, at time t_i^ν, is *synchronized* with the *preceding* AR event μ, of level l or higher, which made landfall at time t_l^μ, if and only if ~~they occurred within the~~ their temporal delay, $t_i^\nu - t_l^\mu \geq 0$, does not exceed the ~~*local (dynamical) coincidence interval*~~*delay* ~~τ_{lm}^{ij}~~ ~~(Quiroga et al., 2002)~~

$$\tau_{lm}^{ij}{}_{l,i}^{\mu,\nu} = \frac{1}{2}\min\left\{t_{l+1}^i{}_l^\mu - t_l^{\mu-1}, t_l^{\mu+1} - t_{l\,l}^{i\,\mu}, t_l^i - t_{l-1}^i{}_i^\nu - t_{m+1}^j - t_{m\,i}^{j\;\nu-1}, t_{m\,i}^{j\;\nu+1} - t_{m-1}^j{}_i^\nu\right\}. \quad (1)$$

~~See Fig. 1 for an illustration of the computation of the dynamic coincidence interval τ_{lm}^{ij}. This dynamical~~ This adaptive lag allows us to consider events in more densely and more sparsely occupied parts of the time series in an ~~adaptive and automated manner~~automated manner, in contrast to the classical lead-lag approach that only allows one lead or lag for the entire time series. As the first and last event of each time series has no preceding or subsequent event, we exclude them from

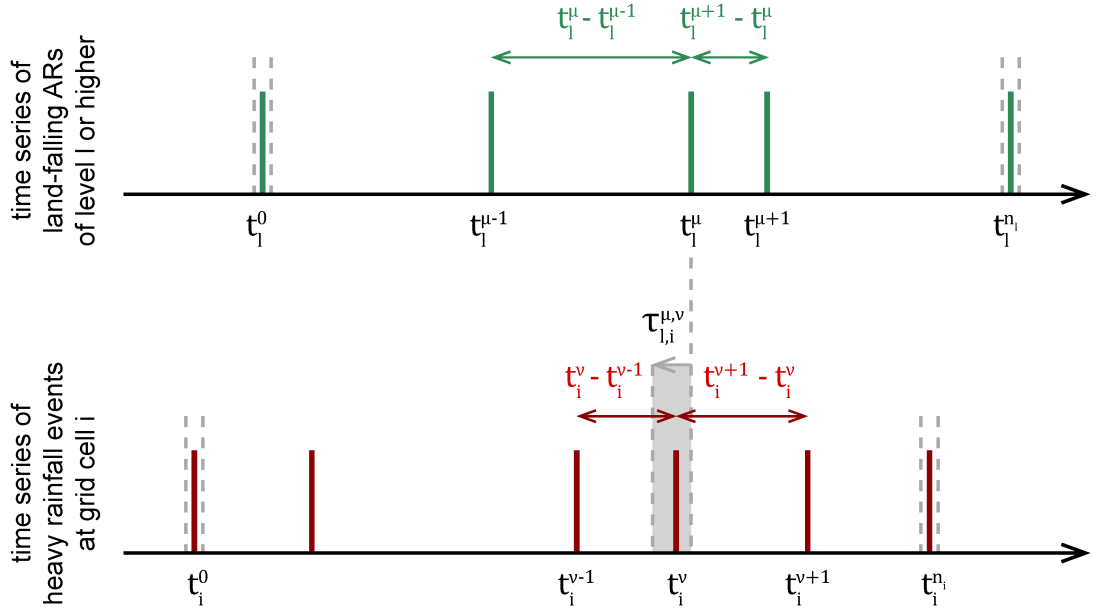

Figure 1. Schematic sketch illustrating event synchronization (ES). Shown is a pair of time series ~~(i,j)~~ and an exemplary computation of the ~~dynamic coincidence interval τ_{lm}^{ij}~~ dynamical delay $\tau_{l,i}^{\mu,\nu}$. Additionally, the first and last events which are not considered for ES are marked by vertical grey lines.

our computations and only consider $\mu = 2, 3, \ldots, n_l - 1$ and $\nu = 2, 3, \ldots, n_i - 1$. See Fig. 1 for an illustration of the computation of the dynamical delay $\tau_{l,i}^{\mu,\nu}$.

To avoid a collapse of the ~~local coincidence interval to $\tau_{lm}^{ij} = \frac{1}{2}$~~ dynamical delay to $\tau_{l,i}^{\mu,\nu} = \frac{1}{2}$ timestep due to sequences of consecutive events, we only consider the first event of all event sequences (cluster-corrected ES) (Boers et al., 2019; Wolf and Donner, 2021).

~~Then, the synchronization condition reads~~

$$\sigma_{lm}^{ij} = \begin{cases} 1, & \text{if } 0 < t_l^i - t_m^j \leq \tau_{lm}^{ij}, \\ 0, & \text{otherwise.} \end{cases}$$

Additionally, we can limit the ~~coincidence interval τ_{lm}^{ij} by a~~ dynamical delay $\tau_{l,i}^{\mu,\nu}$ by a minimal value $\tau_{\min}$ to consider a minimum lag between synchronized events, and also by a maximal value $\tau_{\max}$ to prevent an unrealistically large temporal ~~distance~~ delay between synchronized events. ~~As the first and last event has no preceding or subsequent event, we exclude them from our computations. Thus, we set $l = 2, 3, \ldots, s_i - 1$~~

Then, the synchronization condition reads:

$$S_{l,i}^{\mu,\nu} = \begin{cases} 1, & \text{if } 0 \le t_i^\nu - t_l^\mu \le \tau_{l,i}^{\mu,\nu} \text{ and } \tau_{\min} \le \tau_{l,i}^{\mu,\nu} \le \tau_{\max}, \\ 0, & \text{otherwise,} \end{cases} \tag{2}$$

and for each grid cell i, we define

$$ES_{l,i} = \sum_{\mu=2}^{n_l-1} \sum_{\nu=2}^{n_i-1} S_{l,i}^{\mu,\nu}, \tag{3}$$

as the total number of HPEs that can be uniquely associated with a *preceding* land-falling AR in a time-resolved manner, within an interval of at least $\tau_{\min}$ days and no more than $\tau_{\max}$ days.

Finally, we analyze the statistical significance of each empirical value $ES_{l,i}$, by means of a null model that incorporates 1,000 surrogate pairs of time series of land-falling ARs and HPEs, preserving the original number of events n_l and ~~$m = 2, 3, ..., s_j - 1$~~ n_i respectively, but destroying a potential correlation structure. We calculate the value of $ES_{l,i}$ from the surrogates to estimate an empirical probability distribution, that we then use to infer the significance level of our $ES_{l,i}$ value (Boers et al., 2019). We say that $ES_{l,i}$ is significant at the level $\alpha = 1 - \rho$ if

$$\Theta(ES_{l,i} - ET_\rho(n_l, n_i)) = 1, \tag{4}$$

where ~~s_i and s_j denote the number of events in the time series at location i and j, respectively~~Θ denotes the Heaviside function, and $ET_\rho(n_l, n_i)$ is the $\rho - th$ percentile of the surrogate test distribution for $ES_{i,j}$.

~~Employing the indicator function (Wolf et al., 2020a)~~

$$J_{lm}^{ij} = \begin{cases} 1, & \text{if } \sigma_{lm}^{ij} = 1, \sigma_{m,l-1}^{ji} = 0 \text{ and } \sigma_{m+1,l}^{ji} = 0, \\ \frac{1}{2}, & \text{if either } t_l^i = t_m^j \text{ or } \sigma_{lm}^{ij} = 1 \text{ and } (\sigma_{m,l-1}^{ji} = 1 \text{ or } \sigma_{m+1,l}^{ji} = 1), \\ 0, & \text{otherwise,} \end{cases}$$

~~we calculate the total number of synchronized events by~~

$$c(i|j) = \sum_{l=2}^{s_i-1} \sum_{m=2}^{s_j-1} J_{lm}^{ij}.$$

2.3 Identification of ARs highly synchronized with a specific region

~~The indicator functionassures that pairs~~ One particular advantage of ES is that we can use it to identify the temporal ordering and the time delay of synchronized events~~are not considered in both $c(i|j)$ and $c(j|i)$ (Wolf et al., 2020a). Here, $c(j|i)$ indicates the number of synchronized events where an event at i precedes an event at j~~. From the synchronization condition (see Eq. (2)), note that $S_{l,i}^{\mu,\nu} = 1$ if and only if the land-falling AR event μ precedes and is synchronized with the HPEs event ν observed at

location i. In that case, the time delay between this pair of uniquely associated events is $d_{l,i}^{\mu,\nu} = t_i^\nu - t_l^\mu$. If we use Eq. (4) to only consider the grid cells where the synchronization between land-falling ARs and HPEs is significant, then for a region of interest R, we can define

$$ES_{\mu\to R}^{\rho} = \sum_{i\in R}\sum_{\nu=2}^{n_i-1} S_{l,i}^{\mu,\nu}\Theta(ES_{l,i} - ET_\rho(n_l,n_i)), \tag{5}$$

as the total number of HPEs within R that were preceded and uniquely associated with the land-falling AR μ at the significance level $\alpha = 1-\rho$, during the time window $[\tau_{\min},\tau_{\max}]$ (Boers et al., 2019). Based on this definition, we can retrieve the time delays between the AR event μ and the significantly synchronized HPEs,

$$D_{\mu\to R} := \{d_{l,i}^{\mu,\nu} \mid i\in R \wedge S_{l,i}^{\mu,\nu} = 1 \wedge \Theta(ES_{l,i} - ET_\rho(n_l,n_i)) = 1\}, \tag{6}$$

to define and calculate the *typical synchronization delay* between the AR event μ and the region of interest R as the mode of $D_{\mu\to R}$ (if there are multiple modes, we take the smallest one).

We ~~utilize $c(i|j)$ and $c(j|i)$ to compute the *directed event synchronization strength* as~~

$$q_{ij} = c(i|j) - c(j|i)\,.$$

use this framework to select the ARs of level l or higher with the largest number of significantly synchronized HPEs within the region of interest R and to identify the time points that are then used to compute the composite anomalies of integrated water vapor transport, geopotential height, upper-level meridional wind, and precipitation to be shown in our results.

~~In our work, we use this measure to investigate (a)~~ Even more, we can use Eq. (5) to identify ARs that were not synchronized with HPEs in the region of interest ($ES_{\mu\to R}^{\rho} = 0$). Based on a precedence analysis, we can also identify the dates when HPEs occurred in the region of interest without any AR making landfall on the coast during the previous 12 days (the selection of this preceding time window comes after one of our results). These time points are used to compute composite anomalies of the aforementioned climatological variables, in order to reveal the synoptic conditions that differentiate ARs distributing synchronized HPEs into the region of interest.

2.4 Event Synchronization (ES) between HPEs at different locations

We are also interested in investigating if there is a directed synchronization ~~between ARs~~ pattern between HPEs at different locations in the aftermath of land-falling ARs. Adapting the definition of ES in section 2.2, we consider two HPEs ν and φ in time series describing observations made at grid cells i and j at times t_i^ν and ~~heavy rainfall events and (b)between heavy rainfall events at different locations. For the latter, we use the matrix $\boldsymbol{Q}^{ES}$ (with matrix elements q_{ij}^{ES})~~ t_j^φ as *synchronized* if and only if their temporal delay, $t_j^\varphi - t_i^\nu$, does not exceed the *dynamical delay*

$$\tau_{i,j}^{\nu,\varphi} = \frac{1}{2}\min\left\{t_i^\nu - t_i^{\nu-1}, t_i^{\nu+1} - t_i^\nu, t_j^\varphi - t_j^{\varphi-1}, t_j^{\varphi+1} - t_j^\varphi\right\}. \tag{7}$$

Again, sequences of consecutive events are counted as single events (cluster-corrected ES), and the first and last event of each time series are discarded, i.e. $\nu = 2, 3, \ldots, n_i - 1$ and $\varphi = 2, 3, \ldots, n_j - 1$, where n_i and n_j denote the total number of HPEs at grid cells i and j respectively.

In this case, when the event at i happens before the event at j, the synchronization condition reads:

$$S_{i,j}^{\nu,\varphi} = \begin{cases} 1, & \text{if } 0 < t_j^{\varphi} - t_i^{\nu} \leq \tau_{i,j}^{\nu,\varphi} \text{ and } \tau_{\min} \leq t_j^{\varphi} - t_i^{\nu} \leq \tau_{\max}, \\ 0, & \text{otherwise,} \end{cases} \tag{8}$$

Note the subtle but important difference with Eq. (2), we do not include events that occur at the very same time step at different locations, since we cannot determine their temporal ordering.

We define the directed event synchronization from i to j as

$$ES_{i,j} = \sum_{\nu=2}^{n_i-1} \sum_{\varphi=2}^{n_j-1} S_{i,j}^{\nu,\varphi}, \tag{9}$$

which is the total number of synchronized events where an event at i precedes an event at j by at least $\tau_{\min}$ days and no more than $\tau_{\max}$ days.

The reverse time direction is given by

$$ES_{j,i} = \sum_{\varphi=2}^{n_j-1} \sum_{\nu=2}^{n_i-1} S_{j,i}^{\varphi,\nu}, \tag{10}$$

resulting in the asymmetric matrix $\mathbf{ES}$, which we use for setting up climate networks ~~(see Sect. 2.5).~~ as described in the following section.

2.5 Climate networks

~~In climate networks,~~ Functional networks are defined as graphs where nodes represent the elements of a complex system and edges represent the interaction between them. In functional networks, edges are placed between nodes in accordance with some statistical similarity, regardless of whether the nodes are physically connected or not. A climate network, as introduced in former work by Tsonis and Roebber (2004), Tsonis et al. (2006), and Donges et al. (2009a), ~~links are placed between nodes based upon some statistical association between the time seriesassociated with these nodes~~is a functional network whose nodes are identified with climatological time series, typically measured at specific spatial locations or grid cells~~. Here, we utilize~~ , and whose edges account for a significant and strong correlation between the respective time series. Recently, the climate network approach has attracted much attention after being successfully applied to reveal novel insights into the dynamics of the Earth's climate system, over different spatiotemporal scales (Tsonis and Swanson, 2008; Yamasaki et al., 2008; Donges et al., 2009b, 2011; Malik .

A network consists of N nodes connected by e edges. The topology of such a network is commonly encoded in the adjacency matrix $\mathbf{A}$, with elements $a_{i,j}$ indicating if nodes i and j are connected. In this study, we construct climate networks based on

ES to assess the ~~spatio-temporal~~ spatiotemporal correlation structure of ~~heavy rainfall in NA. For that, we~~ HPEs in NA, and to unravel possibly non-linear and long-ranged climatic linkages associated with the landfall of ARs on the western coast of NA. We identify the nodes of the network with the gridded time series of the ERA5 reanalysis data and connect the nodes based on their statistical association evaluated by ES. To transform the daily ERA5 ~~rainfall~~ precipitation estimates to an event time series, we threshold ~~each time series (located at the grid points) at the 95^{th}~~ the time series of wet days of each grid cell at the 95th percentile. Subsequently, we apply the cluster-corrected ES (Boers et al., 2014a; Wolf et al., 2020a) with ~~an~~ a lower and upper threshold of the dynamical ~~coincidence interval~~ delay which is specified in the respective sections.

~~A network consists of N nodes connected by e edges. The topology of such a network is commonly encoded in the adjacency matrix $\mathbf{A}$ with elements a_{ij} indicating if nodes~~ We use the resulting synchronization matrix $\mathbf{ES}$ to place a directed link pointing from grid cell i ~~and j are connected. In directed networks, as in this work, the adjacency matrix is not symmetric (in contrast to undirected networks), but binary since we do not consider link weights: ($a_{ij} = 1$ if a link points from node j to node~~ to grid cell j if HPEs at i ~~$a_{ij} = 0$ otherwise).~~ precede and are synchronized with HPEs at j.

~~To construct functional climate networks from the resulting matrix $\boldsymbol{Q}^{ES}$,~~ Note that, by construction, we typically have different numbers of events at different grid cells, since we calculate the percentile of the wet days, not of the entire time series. The number of events affects the measured values of ES, therefore, to ensure that the edges placed between nodes are statistically significant, we apply a ~~specifically~~ locally tailored significance testing scheme. For each pair of ~~time series~~grid cells (i, j), we set up a ~~significance test~~ null model using $1,000$ surrogate ~~time series with~~ pairs of time series preserving the respective numbers of events ~~in each time series. We~~ n_i and n_l. We assume that the events at each location occur independently according to a uniform random distribution and compute the values $ES_{i,j}$ and $ES_{j,i}$ for each surrogate pair of time series, obtaining two empirical distribution functions. We then connect nodes in the network (by setting ~~$a_{ij}^{ES} = 1$) if q_{ij}^{ES} exceeds the 99.5^{th}~~ $a_{i,j} = 1$ in the adjacency matrix) if $ES_{i,j}$ exceeds the 99.5th percentile of the respective surrogate test distribution (Boers et al., 2019):

$$a_{i,j} = \Theta\left(ES_{i,j} - ET_{0.995}(n_i, n_j)\right) - \delta_{i,j}, \tag{11}$$

where Θ denotes the Heaviside function, $ET_{0.995}(n_i, n_j)$ is the 99.5th percentile of the surrogate test distribution for $ES_{i,j}$ and Kronecker's delta δ is used to exclude self loops.

As a remark, we want to emphasize that considering the temporal ordering of the events to calculate ES (see Eqs. (9) and (10)), results in a *directed climate network*, for which the adjacency matrix is not symmetric (in contrast to undirected networks). Moreover, since we also do not consider edge weights, the adjacency matrix is binary: $a_{i,j} = 1$ if an edge points from node j to node i, $a_{i,j} = 0$ otherwise.

This methodology of combining ES and complex networks is based on the idea that ARs influence the way HPEs synchronize at different locations, and that these effects are contained in the internal structure of the climate network, which can be accessed by appropriate complex network measures. In many cases, climate networks are a powerful alternative to more traditional approaches based on eigenvalue techniques (e.g., PCA) (Boers et al., 2013). However, the methodology employed here has been specifically developed to analyze time series of climatological extreme events, for which PCA-like methods are not

applicable due to the binary-like structure and the non-Gaussian distributions of the data (Malik et al., 2012; Boers et al., 2013, 2014a, c, b,).

To calculate the number of nodes to which node i is connected, we compute the in-degree k_i^{in} ~~as~~

$$k_i^{in} = \sum_{j=1}^{N} a_{ij},$$

~~and the~~ (out-degree k_i^{out} ~~as~~

$$k_i^{out} = \sum_{j=1}^{N} a_{ji}.$$

) as the total number of links pointing to (from) grid cell i. To aggregate both measures and to ~~especially~~ highlight regions of predominately outgoing (or incoming) connections, we ~~also measure the network divergence~~ define the *network divergence* as

$$d_i = k_i^{out} - k_i^{in} = \sum_{j=1}^{N} a_{ji,j} - \sum_{j=1}^{N} a_{ij,j,i}, \tag{12}$$

with positive (negative) values of d_i indicating sources (sinks) of the network: HPEs in these locations are followed (preceded) by HPEs in other locations.

3 Results and discussion

3.1 ~~Heavy rainfall events~~ HPEs synchronized with strong ARs

As a first step, we investigate where ~~heavy rainfall events~~ HPEs occur synchronized to ~~ARs hitting the coast~~ land-falling ARs and at which lags. For that, we employ ES and evaluate the synchronization between the AR time series and the time series of ~~the heavy rainfall events~~ HPEs at each grid point in the study area. To obtain the latter one, we threshold ~~each rainfall time series~~ the precipitation time series during wet days at the respective 95th percentile. For the former one, we consider ARs ~~hitting the~~ from the SIO-R1 catalog making landfall on the North American west coast at a latitude $\geq 47.5°$N. Initially, we included all ARs but additional analyses showed that our results are predominantly caused by ARs that ~~land-fall~~ landfall north of $47.5°$N (see appendix A, Fig. A1). Moreover, we want to emphasize that our results can be reproduced using an alternative AR catalog based on the IPART algorithm (also featured in appendix A, see Fig. A2). To separate the impact of rather weak ARs from strong ARs, we differentiate between AR ~~categories~~ levels (classification based on Ralph et al. (2019) using the notation in Eiras-Barca et al. (2021)) and run the analysis repeatedly, excluding ARs from lower ~~categories~~levels.

~~Figure ??~~

Figure 2 shows the grid points whose time series of ~~heavy rainfall events have significant ($p < 0.05$) synchronization~~ HPEs are significantly synchronized with the AR time series, given a particular parameter setting of ES and ARs of ~~category~~ level

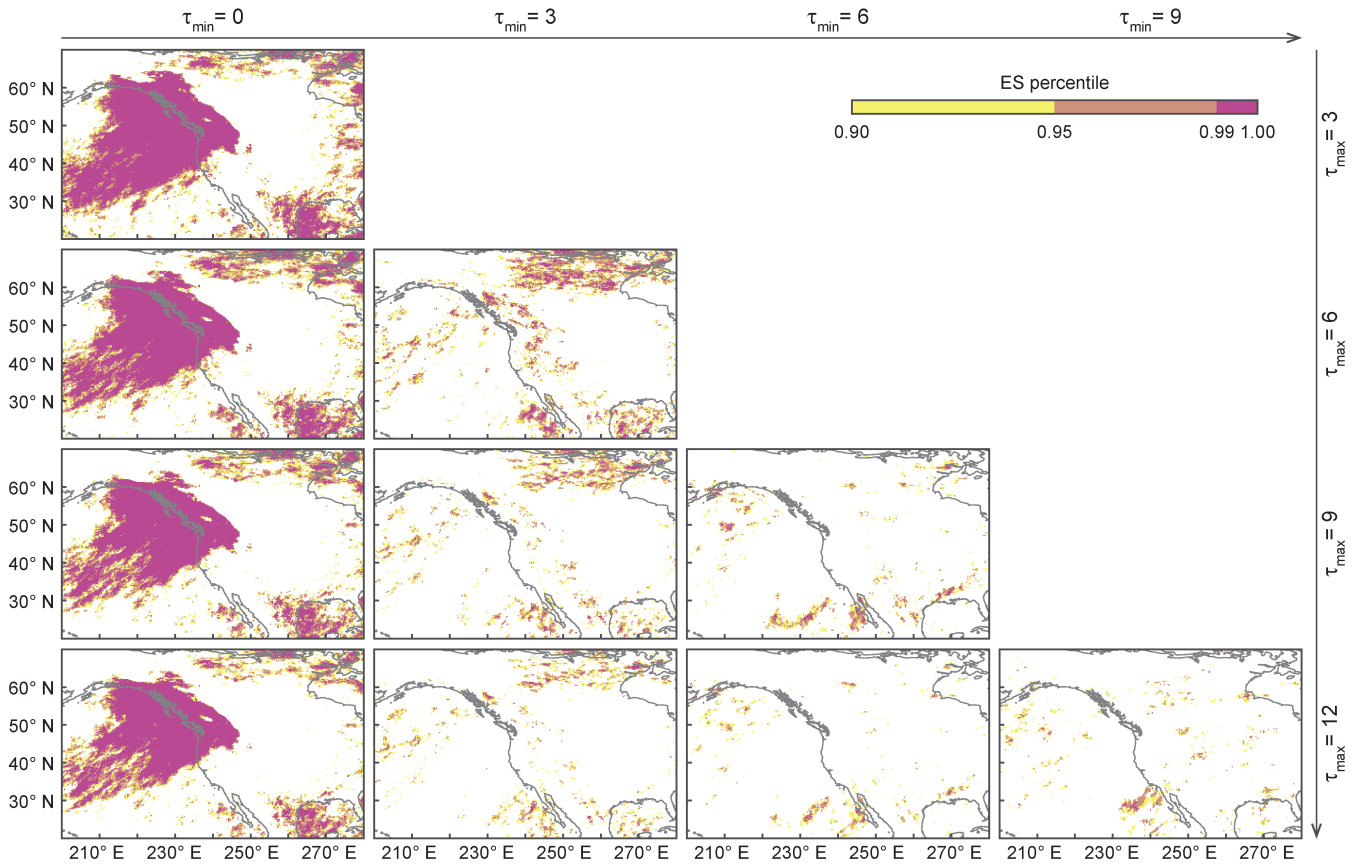

Figure 2. Event synchronization (ES) between ARs making landfall on the western coast of NA and HPEs. We use the SIO-R1 catalog of land-falling ARs but only consider ARs of level AR3 or higher with land-falling latitude north of 47.5°N. Different values of τ_{min} and τ_{max} are considered to calculate ES in each panel: τ_{min} increases from left to right and τ_{max} from top to bottom. Note the irregularly spaced color bar: Yellow indicates high synchronization between HPEs and ARs of level AR3 or higher, at a significance level of $\alpha = 0.1$. Orange indicates high synchronization at a significance level of $\alpha = 0.05$ (and ES percentile > 0.95). Pink indicates high synchronization at a significance level of $\alpha = 0.01$ (and ES percentile > 0.99).

AR3 or higher. ~~We only observe a significant correlation close to the western coast of NA, which is expected but already implied by findings of previous studies, if we also include ARs of lower categories. Therefore, we have selected this subset for our analysis.~~

~~Consequently, when $\tau_{min} = 0$~~ First, note that when $\tau_{min} = 0$ (left column), large areas close to the ~~coast~~ western coast of NA show significant correlations~~as expected. This~~ . This pattern is caused by ~~heavy rainfall events at~~ HPEs on the coast that are directly triggered by ~~the ARs . This pattern~~ ARs and is not affected by increasing ~~τ_{max}~~ τ_{max}. If events occur in close succession, then a higher possible maximal delay will often not be taken into account and, therefore, the pattern does not change visibly. This strong synchronization between land-falling ARs and HPEs on the western coast of NA was expected, as it has already

been implied by findings of previous studies (Neiman et al., 2008; Gershunov et al., 2017; Waliser and Guan, 2017; Ralph et al., 2019), and serves as a proof of concept for our methodology. Excluding ARs of the lower levels AR1 and AR2 does not change this result (see appendix A, Fig. A3). Therefore, we have selected ARs of level AR3 or higher for our analysis.

~~Event synchronization (ES) between time series of heavy rainfall events and the AR time series of the SIO-R1 catalog, considering only ARs of category 3 and higher that land-fell at latitudes $\geq 47.5°$. Different values of τ_{min} and τ_{max} were considered to calculate ES in each panel: τ_{min} increases from left to right and τ_{max} from top to bottom. Note the irregularly spaced color bar: Yellow indicates high, but not significant synchronization between heavy rainfall and ARs of category 3 or higher. Orange indicates significant synchronization with $p < 0.05$ (and ES percentile > 0.95). Pink indicates significant synchronization with $p < 0.01$ (and ES percentile > 0.99).~~

~~When $\tau_{min} = 3$~~ When $\tau_{\text{min}} = 3$ (second column), the synchronization close to the coast ~~is decreased~~decreases, as most ~~heavy rainfall falls~~ HPEs occurs on the first days after an AR ~~strike~~makes landfall. Additionally, most ARs do not persist longer than 3 days (Gershunov et al., 2017). The remaining synchronized events are likely associated with ARs of the higher ~~categories~~ levels which have a longer persistence. Additionally, we observe a patch of synchronized events in central and eastern Canada. This pattern is strongest when ~~$\tau_{min} = 3$ and $\tau_{max} = 12$~~ $\tau_{\text{min}} = 3$ and $\tau_{\text{max}} = 6$ and stands out to a smaller extent ~~for $\tau_{min} = 6$ (third column) and~~ up to $\tau_{\text{max}} = 12$. For elevated values of ~~τ_{max}~~ τ_{min} (third and fourth columns), the synchronization pattern completely vanishes.

This result implies that in central and eastern Canada, ~~heavy rainfall~~ HPEs occurs synchronized (but lagged) to ARs ~~hitting~~ making landfall on the western coast of NA. We, therefore, suspect that moisture that has been transported to the North American west coast by an AR can be channeled to ~~western and central~~ central and eastern Canada and also cause ~~heavy rainfall there~~HPEs there, as hinted in previous studies by Rutz et al. (2014), Waliser and Guan (2017), and Guan and Waliser (2019).

3.2 Synchronization across AR strength

Using ES, we have identified a region of synchronized ~~heavy rainfall events in eastern and central~~ HPEs in central and eastern Canada, as explained in the previous section. To further evaluate how the results depend on the selected ~~category~~ AR-level criteria, we step-wise exclude ARs of the lower ~~categories for the analysis~~levels from the analysis, as shown in Fig. ~~??~~3. Doing this, we reduce the number of events in the AR time series, which heavily affects the outcome of ES. As a result, we find that when we consider all ARs, the signal in central and eastern Canada is present but is ~~less intense and covers a smaller area than previously observed~~ accompanied by a more prominent synchronization pattern right next to the western coast of NA (Fig. ~~??~~). ~~The most extensive pattern is found~~ 2). When we discard low-level ARs, the pattern next to the coast is filtered out and when we take into account ARs of ~~category~~ level AR3 or higher, just the signal in central and eastern Canada is left. Only examining ARs of ~~categories~~ levels AR4 and AR5 leads to a vanishing of the ~~pattern, although rainfall anomalies show heavy rainfall in eastern and central Canada~~ synchronization in central and eastern Canada, although precipitation anomalies show HPEs in that region for composites based on the days after such strong ARs (see appendix A~~). We suspect that this~~, Fig. A6). This is a result of reducing the number of events in the AR time series. Very intense ARs are rare and ~~in this case~~when we only consider them, the AR time series contains very few events. In other words, the AR time series get too sparse ~~for high ES scores , although~~

heavy rainfall and the ES scores are not significant any more, although HPEs might be always caused by such ARs but likely not *just* by them.

Event synchronization (ES) between time series of heavy rainfall events and the AR time series of the SIO-R1 catalog, considering only ARs that land-fell at latitudes $\geq 47.5°$. ES was calculated with $\tau_{min} = 3$ and $\tau_{max} = 12$. From (a) to (e) the considered lower AR category limit increases: (a) ARs of category 1 and higher e.g. all ARs; (b) ARs of category 2 and higher; rest accordingly. Color bar as in Fig. **??**.

3.3 Network analysis of HPEs during AR-days

3.4 Network analysis of heavy rainfall during ARs

In the previous sections, we examined the synchronization between heavy rainfall HPEs and the singular AR time series(constructed via aggregating ARs land-falling north of 47.5° lat). To elaborate further on the concept of synchronized heavy rainfall eventsHPEs, we assess how rainfall precipitation at different locations is organized during AR timesAR-days. For that, we select the days with active ARs of category level AR3 or higherland-falling , making landfall north of 47.5°lat N and the respective subsequent 3 days. We acknowledge that with this approach we can only relate rainfall events HPEs close to the

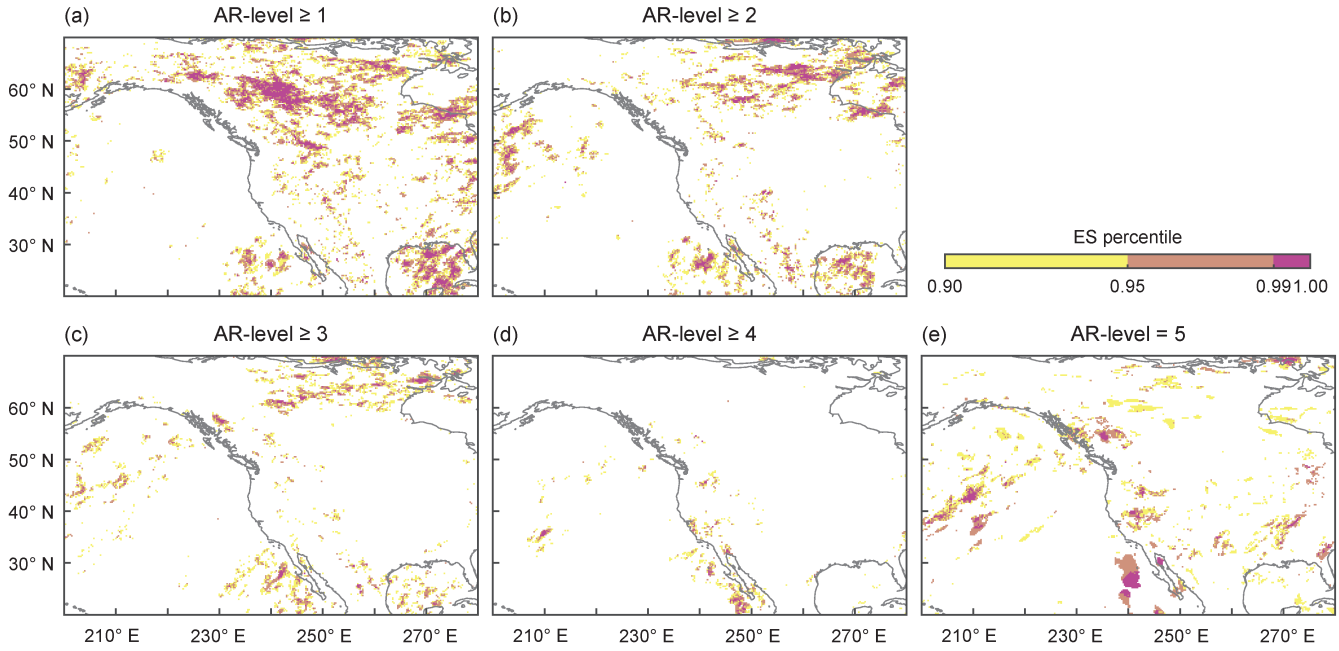

Figure 3. Event synchronization (ES) between ARs making landfall on the western coast of NA and HPEs. We use the SIO-R1 catalog of land-falling ARs but only consider ARs making landfall north of 47.5°N. ES is calculated with $\tau_{min} = 3$ and $\tau_{max} = 12$. From (a) to (e) the lower limit of the considered AR level increases: (a) ARs of level AR1 and higher e.g. all ARs, (b) ARs of level AR2 and higher, rest accordingly. Color bar as in Fig. 2.

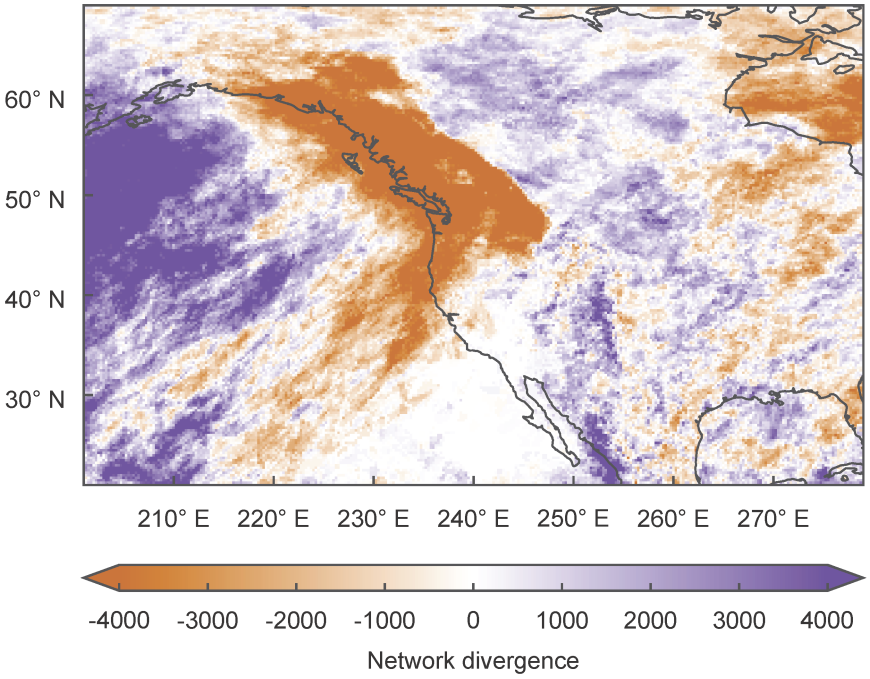

Figure 4. Network divergence based on event synchronization (ES) between ~~heavy rainfall and ARs of category 3 or higher that land-fell~~ HPEs at ~~latitudes $\geq$ 47.5° according to the SIO-R1 catalog~~different locations during AR-days. We calculate ES with $\tau_{\min} = 0$ and $\tau_{\max} = 3$, and we only consider ~~rainfall events~~ HPEs that occurred from 0 to 3 days after ~~the land-falling of~~ an AR ~~and we calculate ES with $\tau_{min} = 0$ and $\tau_{max} = 3$~~of level AR3 or higher makes landfall north of 47.5°N according to the SIO-R1 catalog. In the network, only nodes with significantly directed event synchronization ~~strength were~~ are connected (see ~~Sect~~Sec. ~~2~~ 2.5 for more details). Purple (orange) colors indicate regions with positive (negative) divergence, i.e. nodes with more outgoing (incoming) connections.

coastline to ARs. Based on these selected days, we ~~ran~~ run a network analysis using ES ~~(with the~~ with parameters $\tau_{\min} = 0$, $\tau_{\max} = 3$~~)~~. Therefore, we investigate the immediate synchronization pattern of ~~heavy rainfall events~~ HPEs occurring simultaneously with ARs.

In Fig. ~~??~~ 4 we show the resulting network divergence, which is characterized by a large area of ~~positive values at~~ negative values on the coast overland and ~~negative~~ positive values over the eastern part of the Pacific. Note that network divergence is computed by subtracting ~~*out_degree − in_degree*.Therefore,~~ $k_i^{out} - k_i^{in}$ (out-degree minus in-degree, see Eq. (12)), therefore, areas with positive (negative) values have more outgoing ~~links (sources) and areas with negative values have more incoming links~~ (incoming) edges and can be regarded as sources (sinks) of the network. We identify a clear source in the Pacific ocean and a sink close to the western coast of NA. We find ~~, that rainfall events~~ that HPEs over the Pacific occur first ~~(and are therefore shown as sources), followed by rainfall events~~ and are then followed by HPEs over the western parts of NA~~(hence these regions are marked as sinks)~~. Additionally, ~~it seems as if~~ there is a wave-like pattern hidden in Fig. ~~??~~ 4 (moving further east, we observe another large area of negative network divergence, followed by positive values over the Atlantic and the ~~NA east coast~~ east

coast of NA). Since our filtering only allows for interpreting the dynamics near the western coast of NA, we can only speculate about the causes of this pattern. We suspect that there are either other climate features such as synchronized ARs serving as ~~rainfall~~ precipitation sources in the North ~~(e. g. as described in Mo and Lin (2019))~~ (e. g. as described in Mo and Lin, 2019) or a previous ~~AR strike that caused~~ land-falling AR causing a cascade of synchronized ~~heavy rainfall events~~ HPEs traversing eastwards.

3.4 ~~Synchronization~~ Network analysis of ~~heavy rainfall events~~ HPEs in the aftermath of AR events

After the proof of concept in the previous section, we now extend the spatial and temporal domain. Our initial analysis showed that ~~heavy rainfall events~~ HPEs which occur in central and eastern Canada, are synchronized with ~~AR strikes at~~ ARs land-falling on the western coast of NA considering delays in a window between ~~$\tau_{min} = 3$ and $\tau_{max} = 12$~~ $\tau_{\text{min}} = 3$ and $\tau_{\text{max}} = 12$ (See Fig. ~~??). To now link heavy rainfall events that are triggered by~~ 2). Now, to link HPEs that are related to ARs, we choose the following setup: we consider events that occurred from 0 to 12 days after the ~~land-falling~~ landfall of an AR of at least ~~category~~ level AR3 and employ ES with ~~$\tau_{min} = 3$ and $\tau_{max} = 12$~~$\tau_{\text{min}} = 3$ and $\tau_{\text{max}} = 12$. With that, we assure that we keep ~~heavy rainfall events at~~ HPEs on the coastline and in central and eastern Canada, but only allow synchronization for temporal delays larger than 3 days. ~~With that~~Consequently, we avoid obtaining a strong signal of synchronized events ~~mainly~~ along the western coast of NA (where the main synchronization of events happens during the first 3 days after the first AR day). In other words: we examine the delayed synchronization pattern of ~~heavy rainfall events~~ HPEs (at least 3 days between events) occurring at any time after ~~the land-falling of~~ an intense AR makes landfall. The resulting network divergence is displayed in Fig. ~~??~~5a.

We identify a region of positive network divergence along the northern part of the western coast of NA and especially a region of reduced network divergence over central and eastern Canada, where the synchronization between the AR time series and the ~~heavy rainfall events~~ HPEs was initially discovered. To finally verify that there is a strong connection between the North American west coast, where we find a large number of outgoing ~~links~~edges, and central and eastern Canada, where many ~~links~~ edges terminate, we analyze where ~~links~~ edges that connect to central and eastern Canada originated (see out degree and red box in Fig. ~~??~~5b).

Fig. ~~??~~5b highlights the grid cells where ~~links~~ edges originate that terminate in ~~Central~~ central and eastern Canada (red box). This box has been chosen based on where we have found the synchronization between the AR time series and the ~~heavy rainfall~~ HPEs time series (see Fig. ~~??~~ 2 and Fig. ~~??~~3). One main source of ~~links~~ edges to this region is the North and ~~Northeast~~ Northwest of the study area. This confirms that ~~links~~ edges emerge from the region that is marked by positive values in the network divergence (where ~~heavy rainfall events~~ HPEs synchronized within the first 3 days of ~~an AR strike~~the landfall of an AR) and terminate in the red box.

In summary, we have identified a cascade of ~~heavy rainfall events: in~~ HPEs: on the first 3 days after ~~the first day of an AR strike, rainfall events~~ an AR of level AR3 or higher makes landfall, HPEs are mostly occurring close to or ~~at~~ on the coast and synchronize in this area. In the subsequent days, moisture can be transported to central and eastern Canada and cause ~~heavy rainfall~~ HPEs there. This takes place between 3 and 12 days after the first AR-induced ~~rainfall at~~ precipitation on the coastline.

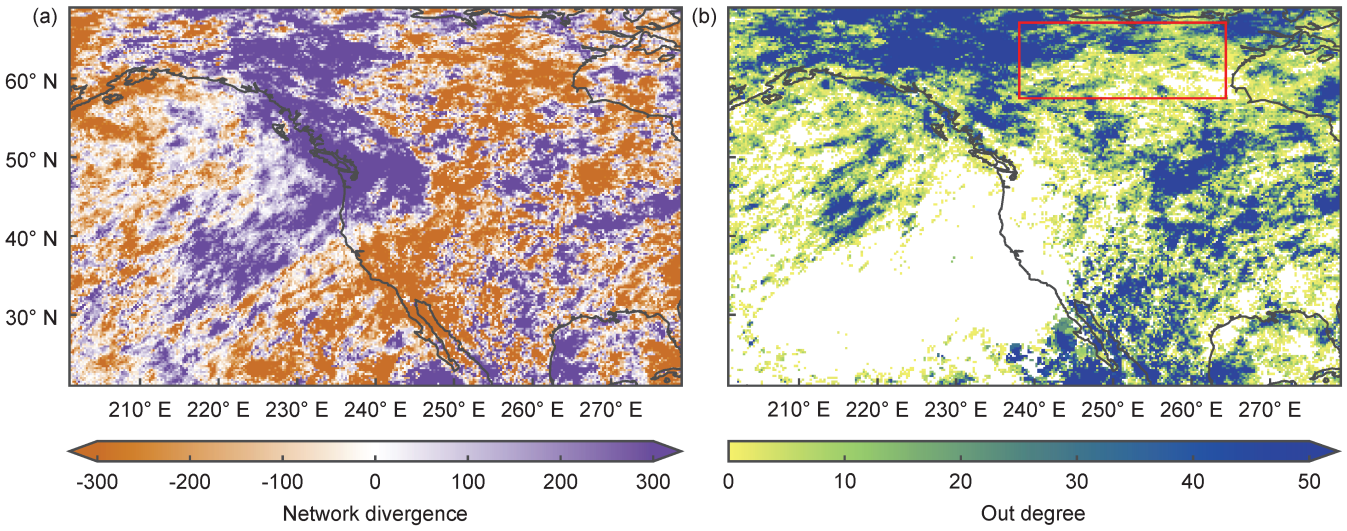

Figure 5. Network analysis based on event synchronization (ES) between HPEs at different locations in the aftermath of land-falling ARs. We calculate ES with $\tau_{min} = 3$ and $\tau_{max} = 12$, and consider all HPEs that occurred from 0 to 12 days after an AR of level AR3 or higher makes landfall north of 47.5°N according to the SIO-R1 catalog. In the networks, only nodes with significantly directed event synchronization are connected (see Sec. 2.5 for more details). (a) Network divergence. Color bar as in Fig. 4. (b) Out degree of a directed network. Highlighted are the grid cells where edges terminating in central and eastern Canada originated (red box). This box was chosen based on the region with significant synchronization between land-falling ARs and HPEs found in Fig. 2 and Fig. 3.

3.5 Synoptic conditions facilitating AR-induced HPEs in central and eastern Canada

3.6 ~~Climatic conditions facilitating AR-induced heavy rainfall in central and eastern Canada~~

Measuring the synchronization between time series revealed the spatial extent as well as the temporal dimensions of ~~rainfall related to ARs.~~ heavy precipitation related to land-falling ARs over NA. A delayed synchronization pattern between ARs making landfall on the western coast of NA and HPEs in central and eastern Canada was identified. To examine the climatic drivers leading to ~~the heavy rainfall~~ this long-ranged correlation, we study the synoptic conditions of different climatological variables for three types of events, defined as follows,

1. type I event: an AR makes landfall on the western coast of NA and synchronizes with HPEs in central and eastern Canada in the subsequent 3 to 12 days.

2. type II event: an AR makes landfall on the western coast of NA but does not synchronize with HPEs in central and eastern Canada in the subsequent 3 to 12 days.

3. type III event: HPEs occur in central and eastern Canada but no AR made landfall on the western coast of NA during the previous 12 days.

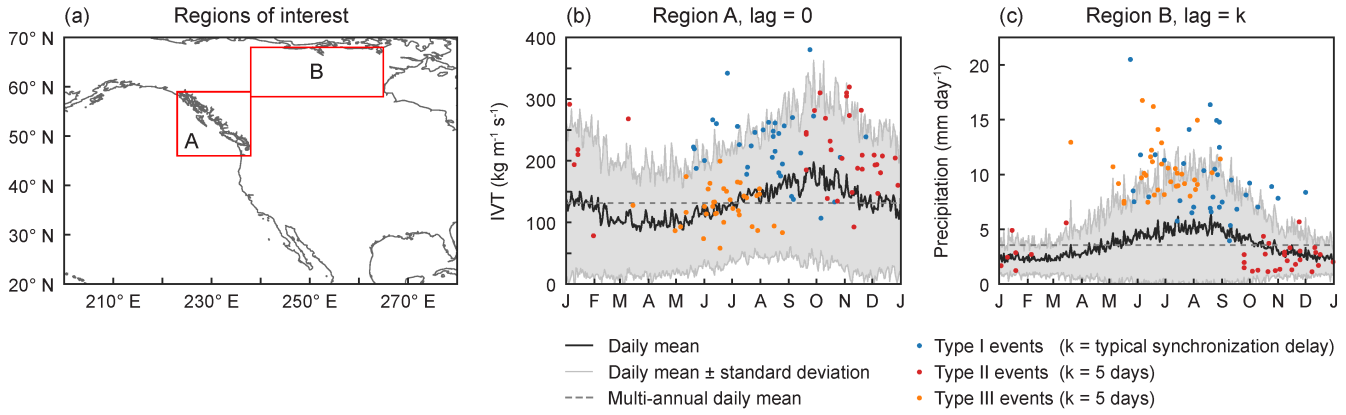

Figure 6. ~~Network analysis based on the event synchronization~~ (~~ES~~a) ~~between heavy rainfall~~ Regions of interest for the study of the synoptic conditions during and ~~ARs~~ after the landfall of ~~category 3 or higher that land-fell at latitudes $\geq$ 47.5° according~~ ARs. Region A (46°N to 59°N latitude and 223°E to 238°E longitude) delimits the ~~SIO-R1 catalog~~area where ARs (with land-falling latitude $\geq 47.5°$) make landfall. ~~We consider all rainfall events that occurred from 0~~ Region B (58°N to ~~12 days after~~ 68°N latitude and 238°E to 265°E longitude) delimits the ~~land-falling~~ area where the delayed synchronization between ARs and HPEs occurs. (b) Annual cycle at daily resolution of ~~an AR~~ the mean IVT in region A (solid dark line). The shading encloses one standard deviation from the daily mean and ~~we calculate ES with $\tau_{min} = 3$ and $\tau_{max} = 12$~~the dashed line indicates the multi-annual mean IVT of the region. ~~In~~ The dots show the ~~networks~~IVT values for days with ARs that synchronize with HPEs (in blue), ~~only nodes~~ days with ~~significantly directed event synchronization strength were connected~~ ARs that do not synchronize with HPEs (~~see Sect. 2 for more details~~in red)~~.~~, and days preceding HPEs without land-falling ARs (~~a~~in orange) ~~Network divergence. Color bar~~ (c) Annual cycle at daily resolution of the mean precipitation in region B, with the same conventions as in ~~Fig. ??.~~ panel (b)~~Out degree of a directed network~~. ~~Highlighted~~ Note that the dots in panel (c) are lagged with respect to the ~~grid cells where links terminating~~ dots in ~~Central and eastern Canada originated~~ panel (~~red box~~b) ~~. This box was chosen based~~ by a value of $k \in \mathbb{N}$ that depends on the ~~region with synchronization between~~ type of event, such that the ~~AR time series~~ dots in panel (b) show the IVT conditions in the western coast of NA and the ~~heavy rainfall time series found~~ dots in ~~Fig~~panel (c) show the subsequent precipitation conditions in central and eastern Canada. ~~??~~ For more details on the types of events and ~~Fig~~the corresponding value of k, see Secs. ~~??~~2.3 and 3.5.

To carefully choose the time points corresponding to each type of event, we first identify specific times with high event synchronization between land-falling ARs and HPEs in central and eastern Canada. We do so by using Eq. (5) with $l = 3$, ~~which is relatively far away from the location where the ARs land-fall, we study different climatological variables.~~ $\rho = 0.9$, $\tau_{\min} = 3$, $\tau_{\max} = 12$ (to match the spatial pattern found in Figs. 2 and 3), and the region of interest as the box in Fig. 5b, which we denote as region B (see Fig. 6a). Note that the resulting $\{ES^{0.9}_{\mu \rightsquigarrow B}\}_{\mu=1,\ldots,n_\mu}$ is a sequence that gives the total number of HPEs in region B that were preceded and uniquely associated with the AR event μ at a significance level $\alpha \leq 0.1$. We identify ARs whose total number of associated HPEs is above the 80th percentile of the nonzero values of this sequence and we get 35 AR events higly synchronized with HPEs in central and eastern Canada. The land-falling times of these ARs are the time points of type I events. We also use Eq. (6) to determine the typical synchronization delay between region B and each of these highly synchronized ARs, with the most common value being 5 days. We then select the 35 most intense AR events for which

$ES^{0.9}_{\mu \rightsquigarrow R} = 0$, i.e. those that did not synchronize with HPEs in central and eastern Canada, and we select their land-falling times as the time points of type II events. Finally, we identify the time points of type III events as the 35 days with the highest number of HPEs in central and eastern Canada that occurred in the absence of land-falling ARs during a time window of 12 precedent days.

~~First, we show IVT anomalies on days with active ARs of category 3 or higher. Additionally, we investigate how the IVT anomalies develop over the respective subsequent days. The high IVT~~ We use these 3 types of events to analyze the antecedent IVT over the western coast of NA and the subsequent precipitation over central and eastern Canada, and thus define the two regions of interest shown in Fig. **??** ~~(top row) is aclear footprint of the ARs. Even after~~ 6a. Region A, where we analyze IVT anomalies, covers the area where the ARs make landfall north of 47.5°N (from 46°N to 59°N latitude and from 223°E to 238°E longitude). Region B, where we study precipitation anomalies, delimits the area where the delayed synchronization pattern between ARs and HPEs was identified (from 58°N to 68°N latitude and from 238°E to 265°E longitude). In Fig 6b we show the annual cycle at daily resolution of the mean IVT in region A (solid dark line). The shading encloses one standard deviation from the daily mean and the dashed line indicates the multi-annual mean IVT of the region. The dots show the IVT values of the 3 types of events previously described. Similarly, Fig 6c shows the annual cycle at daily resolution of the mean precipitation in region B and the precipitation values of the 3 types of events. It is important to clarify that the dots in panel (c) are time-delayed with respect to the dots in panel (b), as follows: *i)* For type I events, the dots in panel (b) are shown on the day the AR makes landfall and the dots in panel (c) are shown after the respective typical synchronization delay ($k \in \{3, 4, \ldots, 12\}$). *ii)* For type II events, the dots in panel (b) are also shown on the day the AR makes landfall but the corresponding dots in panel (c) are shown 5 ~~days (right column)~~days later ($k = 5$). *iii)* For type III events, the dots in panel (b) are shown 5 days before the occurrence of HPEs in central and eastern Canada and the corresponding dots in panel (c) are shown on the day when the HPEs were recorded ($k = 5$).

First, note the clear imprint of ARs on IVT values for type I and II events (Fig 6b, blue and red dots). Whether or not the land-falling AR synchronizes with HPEs in central and eastern Canada, the IVT values in region A are above the daily and the multi-annual mean with very few exceptions. Highly synchronized ARs, corresponding to type I events, have particularly anomalous values of IVT, in most cases exceeding the mean climatology by one standard deviation or more. On the contrary, the IVT values of most type III events (orange dots) are around or below the daily and multi-annual mean IVT of the region, confirming the absence of a precedent AR making landfall on the coast for this type of events. The delayed precipitation over central and eastern Canada associated to each type of events is displayed in Fig. 6. For type I events, as expected, the precipitation values are above the daily and the multi-annual mean, with anomalies that frequently exceed the mean climatology by more than one standard deviation. Conversely, type II events have average or lower precipitation values which is consistent with the absence of a synchronization pattern between land-falling ARs and HPEs. Not surprisingly, type III events referring to HPEs with no precedent ARs also have high precipitation anomalies.

Besides this proof of concept on the effectiveness of our methodology to identify types of events and synchronization delays, Fig. 6 also reveals a key characteristic of the ARs that are highly synchronized with HPEs in central and eastern Canada: their seasonality. These ARs, which define the type I events, occur most likely during July, August, and September,

and can be characterized as intense, long-lasting, ~~there is moisture influx related to the (by then)weakening ARs. The moisture is distributed further to the mainland the higher the delay, but with decreasing intensity.~~ late-summer ARs. Type II events that do not contribute to the observed synchronization pattern in central and eastern Canada, are caused by ARs with similar strength and persistence but making landfall during the early winter, i.e. in October, November, and December. Lastly, type III events describing HPEs that are not preceded by ARs are more common during the early summer months of June, July, and August.

~~Second, the~~ To reveal the synoptic conditions facilitating the delayed effect of ARs in the precipitation over central and eastern Canada, we compute composite anomalies of IVT, geopotential height at 500 ~~hPa geopotential height is assessed for varying delays as for the IVT in the second row of Fig. ??. The strong positive anomalies over the coastline indicate the position of the cyclonic storm causing the AR and the heavy rainfall along the coast. With a higher delay~~ hPa, wind at 500 hPa, and precipitation, on the days of type I events (when the highly synchronized ARs made landfall) and for the following 3, ~~the storm disintegrates slowly while shifting eastwards. Simultaneously, the negative anomalies mainly in the northwestern part of the study area (which correspond to high-pressure areas) also degenerate.~~ 5, and 12 days. The results are shown in Fig. 7. Similar figures for type II and III events can be found in the supplementary material (see appendix A, Figs. A4 and A5).

~~Third, the upper-level (250 hPa)meridional wind anomalies again for the AR-days and the subsequent days are displayed in the third row of Fig. ??. We observe a strong upper-level northward (southward) wind anomaly over the Pacific (continent) . The meridional wind anomalies show the slow disintegration of the cyclonic storm but with a configuration that can guide moisture towards the northern parts of the continent, where we observe the synchronization of the AR time series and the heavy rainfall events .~~

~~Finally, we show rainfall anomalies based on the same parameter setting in the fourth~~ In Fig. 7, we first present the temporal evolution of the IVT anomalies (top row) after the landfall of highly synchronized ARs on the western coast of NA. The high positive IVT anomaly on the Pacific when lag = 0 days is a clear characteristic of land-falling ARs. Noteworthy is that, in the following days, this anomalous water vapor influx is able to penetrate the continent through the topographic gap previously identified by Rutz et al. (2014) and traverses the mainland reaching central and eastern Canada, where the synchronization pattern was found. In the second row of Fig. ~~??. As ARs listed in the employed SIO-R1 catalog~~ 7 the geopotential height at 500 hPa is assessed for varying delays as for the IVT. The trough together with the strong negative anomalies in the northwest of the study region at the moment of land-fall ~~over the western coast, the main region of high rainfall anomalies is close to the west coast~~ indicates the position of the cold front driving the ARs. In the following days, the cold front digs into Canada as a ridge builds in central and eastern United States. This configuration of the geopotential height field during highly synchronized ARs implies a mid-level pressure dipole that traverses the continent accompanied by a southwesterly steering wind (third row of Fig. 7), bringing warm moist air from the western coast into the northern regions of NA. ~~For increasing delay, we observe positive rainfall anomalies in central and eastern Canada~~Under this circumstances, high precipitation anomalies occur just downwind of the trough, first at the coast and then over region B, where we ~~have found the synchronization of the AR time series and the heavy rainfall events. This is in line with the IVT anomaly which maintains an elevated level for higher delays~~identified the delayed synchronization pattern between ARs and HPEs (fourth row of Fig. 7). These synoptic

~~IVT (top row), geopotential height (second row), meridional wind (third row), and rainfall (bottom row) anomalies, from 0 (left column), 3 (middle column), and 5 (right column) days after the first day of land-falling of an AR of category 3 or higher over the western coast of NA at locations north of 47.5°N according to the SIO-R1 catalog.~~

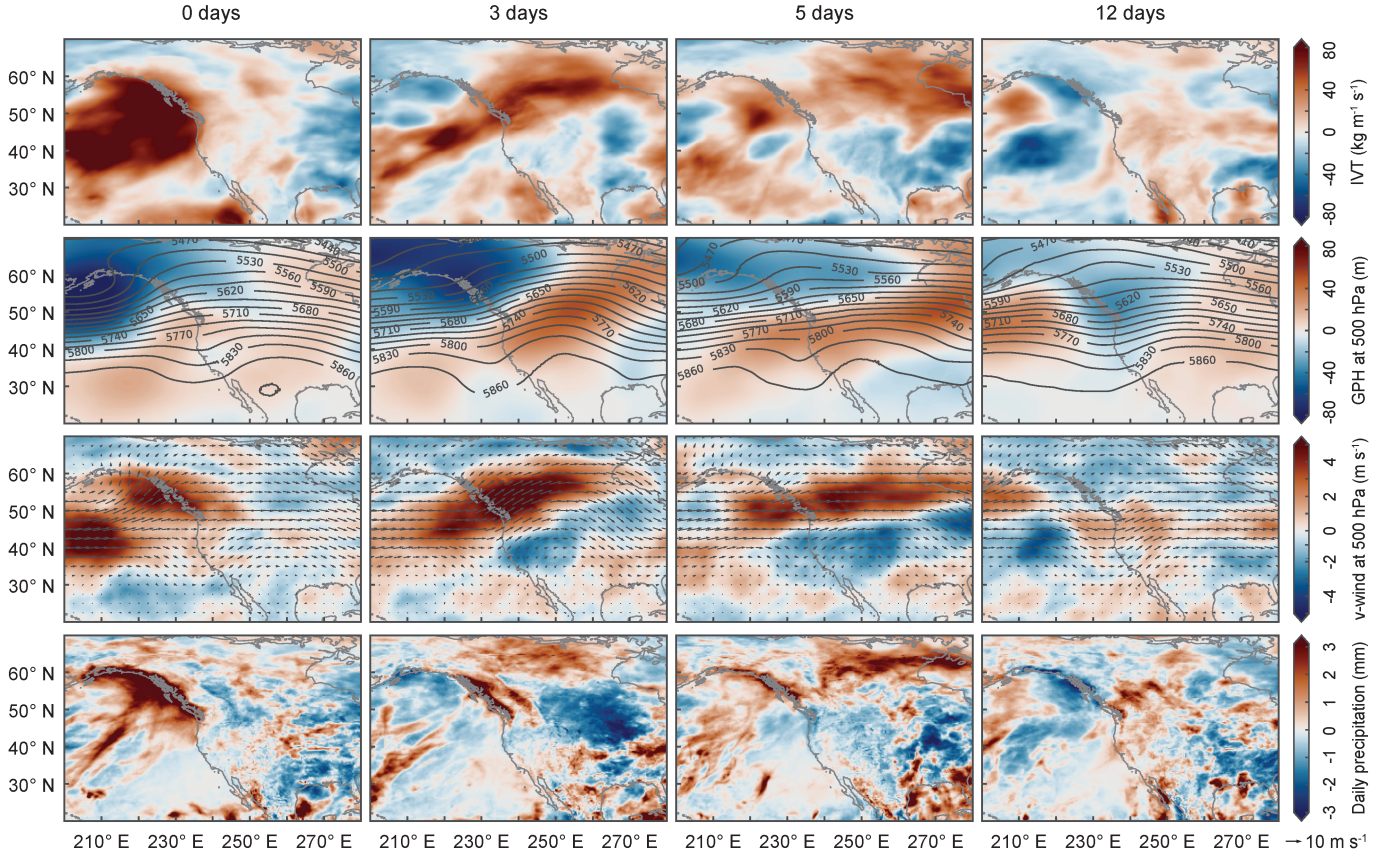

Figure 7. IVT, geopotential height at 500 hPa, wind at 500 hPa, and precipitation anomalies (from top to bottom), from 0, 3, 5, and 12 days (from left to right) after the landfall of ARs leading to a delayed synchronization pattern with HPEs in central and eastern Canada. Only ARs of level AR3 or higher with land-falling latitude north of 47.5°N are considered. In the second row, the shading indicates the anomaly of the geopotential height at 500 hPa and the contours show the mean geopotential height. In the third row, the shading indicates the anomaly of the meridional wind at 500 hPa and the arrows show the mean wind field.

conditions, that are exclusive to highly synchronized ARs (see Figs. A4 and A5) and have already been identified as conducive to the occurrence of seasonal precipitation extremes over Canada (Tan et al., 2019), explain the physical mechanism by which land-falling ARs serve as moisture sources of HPEs in the northern regions of NA.

4 Conclusions

In this study, we have investigated the influence of ARs on the large-scale spatio-temporal synchronization patterns of ~~heavy rainfall over North America (NA)~~HPEs over NA. For this purpose, we have first analyzed if there is a significant association between ARs ~~land-falling at~~ making landfall on the western coast of NA and ~~heavy rainfall events~~ HPEs over the coastal and continental regions. Employing event synchronization (ES), we have revealed timescale-dependent spatial patterns of ~~heavy rainfall which~~ HPEs that are significantly correlated with ~~AR strikes~~ARs making landfall north of 47.5°N: i) immediately after an AR ~~hits~~ makes landfall on the coast, ~~heavy rainfall events~~ HPEs synchronize over the coastal areas. ii) Then, from 3 days after the ~~land-fall~~landfall, the synchronization close to the coast decreases significantly and only ~~heavy rainfall events~~ HPEs associated with more persistent ARs remain. iii) From 3 to 12 days after ~~the first day of an AR strike, heavy rainfall events~~ an AR makes landfall, a synchronization pattern between land-falling ARs and HPEs in central and eastern Canada ~~synchronize with ARs that land-fell north of 47.5°N~~emerges. These results have been reproduced using an alternative AR catalog, establishing the robustness of our findings.

After examining the synchronization of ~~heavy rainfall with singular AR time series~~ HPEs with the time series of land-falling ARs, we have analyzed the organization of ~~heavy rainfall during and after AR strikes~~HPEs on the day of landfall and the subsequent days. For this, we have evaluated ~~ES between the~~ directed ES between time series of ~~heavy rainfall events~~ HPEs at different locations and for different temporal lags after the ~~land-fall of the~~ landfall of ARs. Based on that, we have first constructed a complex network considering a time window from 0 to 3 days after ~~the land-fall of ARs~~landfall. This result confirmed the common knowledge ~~about ARs , namely that heavy rainfall events~~ of the relation between ARs and HPEs in western NA. Initially, HPEs occurring simultaneously with ARs ~~synchronize initially~~ are synchronized over the eastern ~~part of the Pacific Oceanand then are followed by synchronous heavy rainfall events close to~~ Pacific Ocean. They are then followed by synchronized HPEs on the western coast of NA. By examining a second complex network based on ~~heavy rainfall events~~ HPEs occurring at any time after the ~~land-fall~~ landfall of an intense AR, but only allowing synchronization with a delay from 3 to 12 days, we have uncovered a strong connection between ~~heavy rainfall events at~~ HPEs on the North American west coast and ~~at~~ in central and eastern Canada: ~~the moisture of the land-falling ARs~~ moisture from ARs land-falling along the coast can be transported to central and eastern Canada and cause ~~heavy rainfall~~ HPEs there.

To further investigate this result, we ~~have studied the climatic conditions facilitating AR-induced heavy rainfall~~ identified specific days with high event synchronization between land-falling ARs of level AR3 or higher and HPEs in central and eastern Canada. ~~We have constructed the~~ Then, we used these time points to analyze the composite anomalies of vertically integrated water vapor transport (IVT), geopotential height at 500 hPa, ~~upper-level meridional wind , and rainfall, on days with active ARs of category 3 or higher and the respective~~ wind at 500 hPa, and precipitation, on the day of landfall and during the subsequent

3and , 5 days. We have found that IVT can penetrate the continent and reach the northern part of NA , maintaining a moisture influx even 5 days after the land-fall of the ARs. The 500 hPa geopotential height and the meridional wind anomalies showed a circulation pattern that can guide moisture towards the northern parts of the continent . Finally, for increasing delays, we have observed positive rainfall anomalies in and 12 days. Our approach yielded two key findings regarding the climatic conditions that facilitate AR-induced HPEs in central and eastern Canada: *i)* intense, long-lasting, late-summer ARs making landfall north of 47.5°N on the western coast of NA are the ones leading to the occurrence of delayed HPEs in central and eastern Canada, and *ii)* such ARs are driven by a cold front digging from the Northeast Pacific Ocean into Canada as a high-pressure region builds in central and eastern United States. This mid-level pressure dipole traverses the continent accompanied by a southwesterly steering wind, bringing the warm moist air deposited on the coast by the land-falling ARs into central and eastern Canada, where the synchronization of the AR event time series and the heavy rainfall events has been found. and facilitating synchronized but delayed HPEs there. These particular synoptic conditions, that are consistent with the seasonality of the identified ARs, explain the physical mechanism by which late-summer ARs serve as moisture sources of HPEs in the northern regions of NA. However, whether or not these ARs remain as identifiable objects following landfall remains an open question that requires a different catalog than SIO-R1 to be addressed. More specifically, a catalog that tracks the ARs not only until they make landfall, but also as they penetrate the continent.

In summary, we have studied the spatio-temporal synchronization pattern of heavy rainfall HPEs induced by ARs, revealing its extent and its temporal evolution. We have shown that the impact of ARs hitting making landfall on the western coast of NA is not limited to these areas, since they can be accompanied by delayed but significantly synchronized heavy rainfall events HPEs in the continental regions. In particular, we have identified a cascade of heavy rainfall events: in synchronized HPEs: on the first 3 days after the first day of an AR strike, heavy rainfall occurs an AR makes landfall, HPEs occur and synchronize along the coast. In the subsequent days, this moisture can be transported to central and eastern Canada and cause heavy rainfall synchronized HPEs there. Our results illustrate the role of ARs for distributing heavy rainfall over NAand in the distribution of HPEs over NA, not only on the west coast but also over the continental regions through inland penetration of IVT. The findings presented in this work should be considered to better anticipate the evolution of the climate dynamics of the region in the and the associated impacts in the precipitation patterns in the context of a warming atmosphere, where we expect a higher for which we expect an increased frequency and strength of ARs. Since our filtering with the AR time series only allowed us for interpreting the dynamics near the western coast of NA, the physical process by which moisture transported from the coast to the north of the continent causes rainfall there has not yet been identified. Future work could, for example, focus on singular cases of rainfall cascades to uncover the exact mechanisms and provide predictive power for heavy precipitation events in central and eastern Canada triggered by ARs hitting the western coast of NAthe ARs as well as a northward shift of the locations where the ARs make landfall.

Code and data availability. The code is available from the authors upon request. The analysis was conducted with Python and supported by the Python package Pyunicorn Donges et al. (2015). All data sets are publicly available. The ERA5 reanalysis data sets can be downloaded at https://cds.climate.copernicus.eu/. The SIO R1 Catalog can be accessed via https://weclima.ucsd.edu/data-products/.

Author contributions. SV and FW conducted the analysis and wrote the manuscript. SV prepared the figures with the help of FW. DT prepared the section and table for the IPART catalog. All authors reviewed and improved the manuscript. SV conducted the reviews.

Competing interests. The authors declare that they have no competing interests.

Acknowledgements. This research has been funded by the BMBF grant climXtreme (No. 01LP1902J) "Spatial synchronization patterns of ~~heavy precipitation events~~HPEs" and by DFG research training group GRK 2043/1 "Natural risk in a changing world (NatRiskChange)". NB acknowledges funding from the Volkswagen Foundation. SV acknowledges and appreciates the stimulating and fruitful discussions with Dr. Tobias Braun.

Appendix A

A1 ~~Analyzing~~ Analysis of the impact of latitudinally categorized ARs.

In the main manuscript, we have only used ARs ~~land-falling at latitudes $\geq 47.5°$. We have~~ making landfall north of $47.5°$. We based that on the finding that the number of grid cells at which ~~heavy rainfall time series~~ HPEs are significantly correlated with ~~the AR time series is not increasing for including ARs land-falling~~ ARs is not increased by including ARs making landfall at lower latitudes. For that, we have step-wise included more ARs (with a $2.5°$ ~~stepsize~~step size) and counted the number of significant grid cells in central and eastern Canada (for the spatial extent, see red box in Fig. ~~??~~5b). As an illustration of how the results appear ~~for~~ when including all ARs, we have run the analysis evaluating the synchronization between ~~the heavy rainfall time series and the time series of ARs hitting~~ HPEs and ARs making landfall anywhere on the western coast of NA~~somewhere~~. We show Fig. ~~??~~A1, featuring otherwise the same ~~results as~~ key findings as in Fig. ~~??~~2.

As the results shown in Fig. ~~??~~ 2 and Fig. ~~?? are neither~~ A1 are not visually distinguishable in central and eastern Canada ~~nor does~~ and the number of grid ~~points~~ cells exhibiting significant synchronization ~~increase~~does not increase in that region, we assume our choice is robust and proceeded with the subset of ARs for the main analysis.

A2 Dependence on the choice of the AR catalog

As mentioned in the introduction, a plethora of work has analyzed how the choice of an AR detection algorithm affects the outcome of an analysis (Shields et al., 2018; Rutz et al., 2019; O'Brien et al., 2022). For this reason, we have re-run the whole analysis for a systematically different AR catalog (for details see ~~Sect~~Sec. 2). Whereas in the main manuscript we ~~have~~ utilized the SIO-R1 catalog by Gershunov et al. (2017), here we feature the analysis carried out with a catalog based on the IPART algorithm ~~(Xu et al., 2020)~~(Xu et al., 2020; Traxl, 2022).

To verify that we find, in principle, the same results using this alternative approach, we again show the results of assessing the synchronization between ~~the AR time series and~~ land-falling ARs and HPEs, and as in the previous section, we consider all ARs making landfall anywhere on the ~~heavy rainfall time series, this time for all ARs hitting the~~ western coast of NA~~somewhere~~. The results are shown in Fig. ~~??. As expected, the results~~ A2 and, as expected, are visibly different to some extent~~and we have to~~ , so we must acknowledge that we had to adapt the parameters of the analysis. In particular, for the IPART catalog, we reduced the considered lower threshold for the AR ~~category~~level. Therefore, Fig. ~~??~~ A2 is based on ARs of ~~category~~ level AR2 and higher, whereas Fig. ~~??, Fig. ??~~ A1, and Fig. ~~??~~ 2 are based on ARs of ~~category~~ level AR3 and higher. We assume that this is due to two reasons: first, ~~the~~ ARs identified by the IPART catalog have, on average, a shorter persistence in comparison to the ones listed ~~by~~ in the SIO-R1 catalog. Therefore, ~~the~~ ARs are often ~~categorized higher (persistence is one criterion on the AR scale by Ralph et al. (2019))~~ranked higher in the SIO-R1 catalog (persistence is one criterion on the AR scale by Ralph et al., 2019) . Second, the IPART algorithm identified significantly fewer ARs, which leads to a more sparse AR time series. Then, filtering out many ARs may decrease the ES score due to the sparsity of the time series.

Aside from this adaptation, which we consider reasonable, we again ~~, as before,~~ find a region of synchronization between ~~the heavy rainfall time series and the AR time series~~ land-falling ARs and HPEs in central and eastern Canada. Note that the

results show striking qualitative similarity (the signal is strongest for ~~$\tau_{min} \geq 3$ and $\tau_{max} = 12$~~$\tau_{\min} \geq 3$ and $\tau_{\max} = 12$), and for ~~$\tau_{min} \geq 3$~~ $\tau_{\min} \geq 3$ the signal close to the coast vanishes/gets less significant). Therefore, we consider the results based on the IPART catalog (Fig. ~~??~~A2) comparable to the results featured in the main manuscript (Fig. ~~?? and Fig. ??~~2).

~~Event synchronization (ES) between time series of heavy rainfall events and the AR time series of the IPART catalog, considering all ARs of category 2 and higher that land-fell on the western coast of NA. Different values of τ_{min} and τ_{max} were considered to calculate ES in each panel: τ_{min} increases from left to right and τ_{max} from top to bottom. Color bar as in Fig. ??.~~

To be transparent regarding the construction of the IPART catalog we refer to Xu et al. (2020) and the chosen parameters below, which are mostly the default parameters of the algorithm.

A3 Dependence on the choice of the AR level

A4 ~~Rainfall anomalies for increasing AR categories~~

In the main manuscript we have stated that the synchronization pattern observed in the western coast of NA between land-falling ARs and HPEs occurring between 0 and 3 after the landfall does not change if ARs of the lower levels AR1 and AR2 are excluded from the calculations. This statement is based on the results shown in Fig. A3, which displays the grid points whose time series of HPEs are significantly synchronized with the AR time series, when $\tau_{\min} = 0$ and $\tau_{\max} = 3$. In panel (a) all the ARs are considered, and for the subsequent panels, ARs of the lower levels are step-wise excluded such that the lower limit of the considered AR level increases. Note that the most prominent synchronization pattern is always present along the western coast of NA, which is expected given the direct impact of ARs in the inmediate HPEs of this area (Neiman et al., 2008; Gershunov et al., 2017; Wa . However, excluding ARs of the lower levels AR1 and AR2 does not change this result, as only considering ARs from levels AR4 and AR5 does. Including ARs of the lower levels for the calculations of ES introduces noise into the results, especially in eastern NA, where the synchronization pattern is not related to ARs making landfall on the West Coast but rather to ARs and extra-tropical cyclones making landfall on the East Coast. On the other hand, only considering ARs of leves AR4 and AR5 reduces the number of events and makes the AR time series too sparce to retain the statistical significance of the results. Since panel (c) exhibits an intermediate pattern between these 2 scenarios, we have selected ARs of level AR3 or higher for our analysis.

A4 Synoptic conditions during type II and III events

In the main manuscript we revealed the synoptic conditions facilitating the delayed effect of ARs in the precipitation over central and eastern Canada. We did so by analyzing composite anomalies of IVT, geopotential height at 500 hPa, wind at 500 hPa, and precipitation, on the days of type I events (when the highly synchronized ARs made landfall) and for the following 3, 5, and 12 days. Now, we contrast those results with the composite analysis for type II and III events, i.e. for days after the landfall of ARs that did not synchronize with HPEs in central and eastern Canada, and for days before HPEs in central and

Table A1. Parameters used to create the IPART AR catalog.

Parameter name	Short description of the parameter	Parameter value	Unit	Step of the IPART algorithm
kernel	List of integers specifying the shape of the structuring element used in the gray erosion process	$[16, 6, 6]$	-	Top-hat by Reconstruction computation on IVT data
shift_lon	Shifts data along longitude dimension	80	degrees longitude	Top-hat by Reconstruction computation on IVT data
thres_low	Define AR candidates as regions >= this anomalous IVT	1	$kgm^{-1}{}_{s}{}^{-1}$	Detect AR appearances from Top-hat by Reconstruction output
min_area	Drop AR candidates smaller than this area	500.000	km^2	Detect AR appearances from Top-hat by Reconstruction output
max_area	Drop AR candidates larger than this area	$18.000.000$	km^2	Detect AR appearances from Top-hat by Reconstruction output
min_LW	Minimal length to width ratio	2	-	Detect AR appearances from Top-hat by Reconstruction output
min_lat	Exclude ARs whose centroids are lower than this latitude	20	degrees latitude	Detect AR appearances from Top-hat by Reconstruction output
max_lat	Exclude ARs whose centroids are higher than this latitude	80	degrees latitude	Detect AR appearances from Top-hat by Reconstruction output
min_length	ARs shorter than this length are treated as relaxed	$2,000$	km	Detect AR appearances from Top-hat by Reconstruction output
min_length_hard	ARs shorter than this length are discarded	$1,500$	km	Detect AR appearances from Top-hat by Reconstruction output
rdp_thres	Error when simplifying axis using rdp algorithm	2	degrees latitude/longitude	Detect AR appearances from Top-hat by Reconstruction output
fill_radius	Number of grids as radius to fill small holes in AR contour	4	-	Detect AR appearances from Top-hat by Reconstruction output
single_dome	Do peak partition or not, used to separate systems that are merged together with an outer contour	False	-	Detect AR appearances from Top-hat by Reconstruction output
edge_eps	Minimal proportion of flux component in a direction to total flux to allow edge building in that direction	0.4	-	Detect AR appearances from Top-hat by Reconstruction output
zonal_cyclic	Whether to treat the data as zonally cyclic	True	-	Detect AR appearances from Top-hat by Reconstruction output
TIME_GAP_ALLOW	Gap allowed to link 2 ARs	6	hours	Track ARs at individual time steps to form tracks
TRACK_SCHEME	Tracking scheme	simple	-	Track ARs at individual time steps to form tracks
MAX_DIST_ALLOW	Maximal Hausdorff distance to define a neighborhood relationship	1200	km	Track ARs at individual time steps to form tracks
MIN_DURATION	Minimal duration to keep a track	0	hours	Track ARs at individual time steps to form tracks
MIN_NONRELAX	Minimal number of non-relaxed records in a track to keep a track.	0	-	Track ARs at individual time steps to form tracks

eastern Canada that occurred in the absence of a land-falling AR (see Sec. 3.5 for a detailed description of the types of events).

In Fig. A4, we first present temporal evolution of the synoptic conditions after the landfall of ARs that did not synchronize with HPEs in central and eastern Canada. As in Fig. 7, when lag = 0 days, there is a high positive IVT anomaly on the Northeastern Pacific accompanied by a cold front and a southwesterly steering wind driving the ARs to the western coast of NA. Moreover, on the day of landfall, the mid-level pressure dipole identified in Fig. 7 is present and determines the location of HPEs along the western coast of NA. However, the striking difference between ARs leading to type II events and those leading to type I events is the evolution of this pressure dipole in the days following landfall. Note that the cold front vanishes instead of digging into Canada, preventing the anomalous influx of water vapor from reaching the northern parts of North America, and therefore resulting in the absence of HPEs in central and eastern Canada.

Secondly, in Fig. A5 we present the temporal evolution of the synoptic conditions preceding HPEs in central and eastern Canada that occurred in the absence of land-falling ARs. Note the negative IVT, wind, and precipitation anomalies that are always present over the Northeastern Pacific and the western coast of NA, which are attributable to the warm front located in the northwest of the scene. These specific synoptic conditions are a clear indicator of the absence of land-falling ARs during the 12 precedent days considered for the analysis. For type III events, the climatological drivers are more likely related to summertime convective processes forced by the trough located over central Canada when the HPEs occur (right column) (Raddatz and Hanesiak, 2008).

A5 Precipitation anomalies for increasing AR levels

As stated in the main manuscript, only considering ARs of ~~category~~ level AR4 and higher~~or even only examining only category 5 ARs~~ , or even examining only ARs of level AR5, does not lead to significant correlation between ~~the AR time series and the heavy rainfall events~~land-falling ARs and HPEs. We suspect that first, the sparsity of the time series does not allow for significant ES scores but also that ~~heavy rainfall events~~ HPEs do not *only* occur after such strong ARs. To give an argument that these ARs still contribute to the ~~heavy rainfall events~~HPEs, we studied the ~~rainfall~~ precipitation anomalies in the aftermath of just these exceptional AR events. The results are shown in Fig. A6.

Here, as in Fig. ~~??~~7, the delay grows from left to right and the intensity increases from top to bottom. As there are only a few events, the pattern differs visibly between the different parameter settings, but nearly all configurations show a considerable signal of above-average ~~rainfall~~ precipitation in central and eastern Canada. Therefore, we conclude that these strong AR events are one integral part of the ~~found rainfall~~ identified precipitation scheme but explain only one puzzle piece and, thus, do not ~~explain,~~ account just by themselves ~~, the increased rainfall~~ for the increased precipitation in central and eastern Canada.

References

Adhikari, A. and Behrangi, A.: Assessment of satellite precipitation products in relation with orographic enhancement over the western United States, Earth and Space Science, 9, e2021EA001 906, 2022.

Agarwal, A., Marwan, N., Ozturk, U., and Maheswaran, R.: Unfolding Community Structure in Rainfall Network of Germany Using Complex Network-Based Approach, Springer Singapore, https://doi.org/10.1007/978-981-13-2038-5, 2019.

Baggett, C. F., Lee, S., and Feldstein, S.: An investigation of the presence of atmospheric rivers over the North Pacific during planetary-scale wave life cycles and their role in Arctic warming, J. Atmos. Sci., 73, 4329–4347, https://doi.org/10.1175/JAS-D-16-0033.1, 2016.

Baggett, C. F., Barnes, E. A., Maloney, E. D., and Mundhenk, B. D.: Advancing atmospheric river forecasts into subseasonal-to-seasonal time scales, Geophys. Res. Lett., 44, 7528–7536, https://doi.org/10.1002/2017GL074434, 2017.

Boers, N., Bookhagen, B., Marwan, N., Kurths, J., and Marengo, J. A.: Complex networks identify spatial patterns of extreme rainfall events of the South American Monsoon System, Geophys. Res. Lett., 40, 4386–4392, https://doi.org/10.1002/grl.50681, 2013.

Boers, N., Bookhagen, B., Barbosa, H. M. J., Marwan, N., Kurths, J., and Marengo, J. A.: Prediction of extreme floods in the eastern Central Andes based on a complex networks approach, Nat. Commun., 5, 5199, 2014a.

Boers, N., Donner, R. V., and Bookhagen, B.: Complex network analysis helps to identify impacts of the El Niño Southern Oscillation on moisture divergence in South America, Clim. Dyn., 45, 619–632, https://doi.org/10.1007/s00382-014-2265-7, 2014b.

Boers, N., Rheinwalt, A., Bookhagen, B., Barbosa, H. M. J., Marwan, N., Marengo, J. A., and Kurths, J.: The South American rainfall dipole: A complex network analysis of extreme events, Geophys. Res. Lett., 41, 7397–7405, 2014c.

Boers, N., Bookhagen, B., Marwan, N., and Kurths, J.: Spatiotemporal characteristics and synchronization of extreme rainfall in South America with focus on the Andes Mountain range, Clim. Dyn., 46, 601–617, https://doi.org/10.1007/s00382-015-2601-6, 2015.

Boers, N., Goswami, B., Rheinwalt, A., Bookhagen, B., Hoskins, B., and Kurths, J.: Complex networks reveal global pattern of extreme-rainfall teleconnections, Nature, 566, 373–377, https://doi.org/10.1038/s41586-018-0872-x, 2019.

Corringham, T. W., Martin Ralph, F., Gershunov, A., Cayan, D. R., and Talbot, C. A.: Atmospheric rivers drive flood damages in the western United States, Sci. Adv., 5, https://doi.org/10.1126/sciadv.aax4631, 2019.

Dettinger, M. D., Ralph, F. M., Das, T., Neiman, P. J., and Cayan, D. R.: Atmospheric rivers, floods and the water resources of California, Water, 3, 445–478, https://doi.org/10.3390/w3020445, 2011.

Donges, J. F., Zou, Y., Marwan, N., and Kurths, J.: The backbone of the climate network, EPL, 87, 48 007, 2009a.

Donges, J. F., Zou, Y., Marwan, N., and Kurths, J.: Complex networks in climate dynamics, Eur. Phys. J. Spec. Top., 174, 157–179, https://doi.org/10.1140/epjst/e2009-01098-2, 2009b.

Donges, J. F., Schultz, H. C. H., Marwan, N., Zou, Y., and Kurths, J.: Investigating the topology of interacting networks: Theory and application to coupled climate subnetworks, Eur. Phys. J. B, 84, 635–651, https://doi.org/10.1140/epjb/e2011-10795-8, 2011.

Donges, J. F., Heitzig, J., Beronov, B., Wiedermann, M., Runge, J., Feng, Q. Y., Stolbova, V., Donner, R. V., Marwan, N., Dijkstra, H. A., and Kurths, J.: Unified functional network and nonlinear time series analysis for complex systems science: The pyunicorn package, Chaos, 25, https://doi.org/10.1063/1.4934554, 2015.

ECMWF: ERA5: Fifth generation of ECMWF atmospheric reanalyses of the global climate, Copernicus Climate Change Service Climate Data Store (CDS), access: Feb 22 2021, 2021.

Eiras-Barca, J., Ramos, A. M., Pinto, J. G., Trigo, R. M., Liberato, M. L., and Miguez-Macho, G.: The concurrence of atmospheric rivers and explosive cyclogenesis in the North Atlantic and North Pacific basins, Earth Syst. Dyn., 9, 91–102, https://doi.org/10.5194/esd-9-91-2018, 2018.

Eiras-Barca, J., Ramos, A. M., Algarra, I., Vázquez, M., Dominguez, F., Miguez-Macho, G., Nieto, R., Gimeno, L., Taboada, J., and Ralph, F. M.: European West Coast atmospheric rivers: A scale to characterize strength and impacts, Weather and Climate Extremes, 31, 100 305, 2021.

Gao, J., Barzel, B., and Barabási, A.-l.: Universal resilience patterns in complex networks, Nature, 530, 307–312, https://doi.org/10.1038/nature16948, 2016.

Gao, Y., Lu, J., Leung, L. R., Yang, Q., Hagos, S., and Qian, Y.: Dynamical and thermodynamical modulations on future changes of landfalling atmospheric rivers over western North America, Geophys. Res. Lett., 42, 7179–7186, https://doi.org/10.1002/2015GL065435, 2015.

Gershunov, A., Shulgina, T., Ralph, F. M., Lavers, D. A., and Rutz, J. J.: Assessing the climate-scale variability of atmospheric rivers affecting western North America, Geophys. Res. Lett., 44, 7900–7908, https://doi.org/10.1002/2017GL074175, 2017.

Gershunov, A., Shulgina, T., Clemesha, R. E., Guirguis, K., Pierce, D. W., Dettinger, M. D., Lavers, D. A., Cayan, D. R., Polade, S. D., Kalansky, J., and Ralph, F. M.: Precipitation regime change in Western North America: The role of Atmospheric Rivers, Sci. Rep., 9, https://doi.org/10.1038/s41598-019-46169-w, 2019.

Guan, B. and Waliser, D. E.: Detection of atmospheric rivers: Evaluation and application of an algorithm for global studies, Journal of Geophysical Research: Atmospheres, 120, 12 514–12 535, 2015.

Guan, B. and Waliser, D. E.: Tracking atmospheric rivers globally: Spatial distributions and temporal evolution of life cycle characteristics, Journal of Geophysical Research: Atmospheres, 124, 12 523–12 552, 2019.

Guirguis, K., Gershunov, A., DeFlorio, M. J., Shulgina, T., Delle Monache, L., Subramanian, A. C., Corringham, T. W., and Ralph, F. M.: Four atmospheric circulation regimes over the North Pacific and their relationship to California precipitation on daily to seasonal timescales, Geophysical Research Letters, 47, e2020GL087 609, 2020.

Hagos, S. M., Leung, L. R., Yoon, J.-h., Lu, J., and Gao, Y.: North America from the Large Ensemble, Geophys. Res. Lett., 43, 1357–1363, https://doi.org/10.1002/2015GL067392.Received, 2016.

Hersbach, H., Bell, B., Berrisford, P., Hirahara, S., Horányi, A., Muñoz-Sabater, J., Nicolas, J., Peubey, C., Radu, R., Schepers, D., et al.: The ERA5 global reanalysis, Quarterly Journal of the Royal Meteorological Society, 146, 1999–2049, 2020.

Huang, H., Patricola, C. M., Bercos-Hickey, E., Zhou, Y., Rhoades, A., Risser, M. D., and Collins, W. D.: Sources of Subseasonal-To-Seasonal Predictability of Atmospheric Rivers and Precipitation in the Western United States, Journal of Geophysical Research: Atmospheres, 126, e2020JD034 053, 2021.

Huning, L. S., Margulis, S. A., Guan, B., Waliser, D. E., and Neiman, P. J.: Implications of detection methods on characterizing atmospheric river contribution to seasonal snowfall across Sierra Nevada, USA, Geophysical Research Letters, 44, 10–445, 2017.

Krichak, S. O., Barkan, J., Breitgand, J. S., Gualdi, S., and Feldstein, S. B.: The role of the export of tropical moisture into midlatitudes for extreme precipitation events in the Mediterranean region, Theor. Appl. Climatol., 121, 499–515, https://doi.org/10.1007/s00704-014-1244-6, 2015.

Lavers, D. A. and Villarini, G.: The nexus between atmospheric rivers and extreme precipitation across Europe, Geophys. Res. Lett., 40, 3259–3264, https://doi.org/10.1002/grl.50636, 2013.

Lora, J. M., Shields, C., and Rutz, J.: Consensus and disagreement in atmospheric river detection: ARTMIP global catalogues, Geophysical Research Letters, 47, e2020GL089 302, 2020.

Mahoney, K., Swales, D., Mueller, M. J., Alexander, M., Hughes, M., and Malloy, K.: An examination of an inland-penetrating atmospheric river flood event under potential future thermodynamic conditions, Journal of Climate, 31, 6281–6297, 2018.

Malik, N., Bookhagen, B., Marwan, N., and Kurths, J.: Analysis of spatial and temporal extreme monsoonal rainfall over South Asia using complex networks, Clim. Dyn., 39, 971–987, https://doi.org/10.1007/s00382-011-1156-4, 2012.

Messier, C., Bauhus, J., Doyon, F., Maure, F., Sousa-Silva, R., Nolet, P., Mina, M., Aquilué, N., Fortin, M.-J., and Puettmann, K.: The functional complex network approach to foster forest resilience to global changes, Forest Ecosystems, 6, 1–16, 2019.

Mo, R. and Lin, H.: Tropical–mid-latitude interactions: Case study of an inland-penetrating atmospheric river during a major winter storm over North America, Atmosphere-Ocean, 57, 208–232, 2019.

Mundhenk, B. D., Barnes, E. A., Maloney, E. D., and Baggett, C. F.: Skillful empirical subseasonal prediction of landfalling atmospheric river activity using the Madden–Julian oscillation and quasi-biennial oscillation, npj Clim. Atmos. Sci., 1, 19–21, https://doi.org/10.1038/s41612-017-0008-2, 2018.

Neiman, P. J., Ralph, F. M., Wick, G. A., Lundquist, J. D., and Dettinger, M. D.: Meteorological characteristics and overland precipitation impacts of atmospheric rivers affecting the West coast of North America based on eight years of SSM/I satellite observations, J. Hydrometeorol., 9, 22–47, https://doi.org/10.1175/2007JHM855.1, 2008.

Newell, R. E., Newell, N. E., Zhu, Y., and Scott, C.: Tropospheric rivers?–A pilot study, Geophysical research letters, 19, 2401–2404, 1992.

Newman, M., Kiladis, G. N., Weickmann, K. M., Ralph, F. M., and Sardeshmukh, P. D.: Relative contributions of synoptic and low-frequency eddies to time-mean atmospheric moisture transport, including the role of atmospheric rivers, J. Clim., 25, 7341–7361, https://doi.org/10.1175/JCLI-D-11-00665.1, 2012.

O'Brien, T. A., Wehner, M. F., Payne, A. E., Shields, C. A., Rutz, J. J., Leung, L. R., Ralph, F. M., Collow, A. B. M., Guan, B., Lora, J. M., et al.: Increases in Future AR Count and Size: Overview of the ARTMIP Tier 2 CMIP5/6 Experiment, Earth and Space Science Open Archive ESSOAr, 2020.

Ozturk, U., Malik, N., Cheung, K., Marwan, N., and Kurths, J.: A network - based comparative study of extreme tropical and frontal storm rainfall over Japan, Clim. Dyn., 53, 521–532, https://doi.org/10.1007/s00382-018-4597-1, 2019.

O'Brien, T. A., Wehner, M. F., Payne, A. E., Shields, C. A., Rutz, J. J., Leung, L.-R., Ralph, F. M., Collow, A., Gorodetskaya, I., Guan, B., et al.: Increases in future AR count and size: Overview of the ARTMIP Tier 2 CMIP5/6 experiment, Journal of Geophysical Research: Atmospheres, 127, e2021JD036 013, 2022.

Pan, M. and Lu, M.: A novel atmospheric river identification algorithm, Water Resources Research, 55, 6069–6087, 2019.

Payne, A. E., Demory, M.-E., Leung, L. R., Ramos, A. M., Shields, C. A., Rutz, J. J., Siler, N., Villarini, G., Hall, A., and Ralph, F. M.: Responses and impacts of atmospheric rivers to climate change, Nat. Rev. Earth Environ., 1, 143–157, https://doi.org/10.1038/s43017-020-0030-5, 2020.

Prabhat, Kashinath, K., Mudigonda, M., Kim, S., Kapp-Schwoerer, L., Graubner, A., Karaismailoglu, E., von Kleist, L., Kurth, T., Greiner, A., Mahesh, A., Yang, K., Lewis, C., Chen, J., Lou, A., Chandran, S., Toms, B., Chapman, W., Dagon, K., Shields, C. A., O'Brien, T., Wehner, M., and Collins, W.: ClimateNet: an expert-labeled open dataset and deep learning architecture for enabling high-precision analyses of extreme weather, Geoscientific Model Development, 14, 107–124, https://doi.org/10.5194/gmd-14-107-2021, 2021.

Quiroga, R. Q., Kreuz, T., and Grassberger, P.: Event synchronization: A simple and fast method to measure synchronicity and time delay patterns, Phys. Rev. E, 66, 041 904, https://doi.org/10.1103/PhysRevE.66.041904, 2002.

Raddatz, R. and Hanesiak, J.: Significant summer rainfall in the Canadian Prairie Provinces: modes and mechanisms 2000–2004, International Journal of Climatology: A Journal of the Royal Meteorological Society, 28, 1607–1613, 2008.

Ralph, F. M. and Dettinger, M. D.: Storms, floods, and the science of atmospheric rivers, Eos (Washington. DC)., 92, 265–266, https://doi.org/10.1029/2011EO320001, 2011.

Ralph, F. M., Rutz, J. J., Cordeira, J. M., Dettinger, M., Anderson, M., Reynolds, D., Schick, L. J., and Smallcomb, C.: A scale to characterize the strength and impacts of atmospheric rivers, Bull. Am. Meteorol. Soc., 100, 269–289, https://doi.org/10.1175/BAMS-D-18-0023.1, 2019.

Ramos, A. M., Nieto, R., Tomé, R., Gimeno, L., Trigo, R. M., Liberato, M. L., and Lavers, D. A.: Atmospheric rivers moisture sources from a Lagrangian perspective, Earth Syst. Dyn., 7, 371–384, https://doi.org/10.5194/esd-7-371-2016, 2016.

Ramseyer, C. A. and Teale, N.: On the emerging global relevance of atmospheric rivers and impacts on landscapes and water resources, Progress in Physical Geography: Earth and Environment, 45, 965–978, 2021.

Rivoire, P., Martius, O., and Naveau, P.: A comparison of moderate and extreme ERA-5 daily precipitation with two observational data sets, Earth and Space Science, 8, e2020EA001 633, 2021.

Rutz, J. J., Steenburgh, W. J., and Ralph, F. M.: Climatological characteristics of atmospheric rivers and their inland penetration over the western United States, Monthly Weather Review, 142, 905–921, 2014.

Rutz, J. J., Shields, C. A., Lora, J. M., Payne, A. E., Guan, B., Ullrich, P., O'brien, T., Leung, L. R., Ralph, F. M., Wehner, M., et al.: The atmospheric river tracking method intercomparison project (ARTMIP): quantifying uncertainties in atmospheric river climatology, Journal of Geophysical Research: Atmospheres, 124, 13 777–13 802, 2019.

Sharma, A. R. and Déry, S. J.: Contribution of Atmospheric Rivers to Annual, Seasonal, and Extreme Precipitation Across British Columbia and Southeastern Alaska, J. Geophys. Res. Atmos., 125, 1–21, https://doi.org/10.1029/2019JD031823, 2020.

Shields, C. A. and Kiehl, J. T.: Atmospheric river landfall-latitude changes in future climate simulations, Geophysical Research Letters, 43, 8775–8782, 2016.

Shields, C. A., Rutz, J. J., Leung, L.-Y., Ralph, F. M., Wehner, M., Kawzenuk, B., Lora, J. M., McClenny, E., Osborne, T., Payne, A. E., et al.: Atmospheric river tracking method intercomparison project (ARTMIP): project goals and experimental design, Geoscientific Model Development, 11, 2455–2474, 2018.

Smith, B. L., Yuter, S. E., Neiman, P. J., and Kingsmill, D. E.: Water vapor fluxes and orographic precipitation over northern california associated with a landfalling atmospheric river, Mon. Weather Rev., 138, 74–100, https://doi.org/10.1175/2009MWR2939.1, 2010.

Steinhaeuser, K., Ganguly, A. R., and Chawla, N. V.: Multivariate and multiscale dependence in the global climate system revealed through complex networks, Climate dynamics, 39, 889–895, 2012.

Stolbova, V., Martin, P., Bookhagen, B., Marwan, N., and Kurths, J.: Topology and seasonal evolution of the network of extreme precipitation over the Indian subcontinent and Sri Lanka, Nonlinear Process. Geophys., 21, 901–917, https://doi.org/10.5194/npg-21-901-2014, 2014.

Tan, X., Gan, T. Y., and Chen, Y. D.: Synoptic moisture pathways associated with mean and extreme precipitation over Canada for summer and fall, Climate Dynamics, 52, 2959–2979, 2019.

Traxl, D.: dominiktraxl/artracks: Release v1.0.0, https://doi.org/10.5281/zenodo.7130642, 2022.

Tsonis, A. A. and Roebber, P. J.: The architecture of the climate network, Phys. A, 333, 497–504, 2004.

Tsonis, A. A. and Swanson, K. L.: Topology and predictability of El Niño and la Niña Networks, Phys. Rev. Lett., 100, 1–4, https://doi.org/10.1103/PhysRevLett.100.228502, 2008.

Tsonis, A. A., Swanson, K. L., and Roebber, P. J.: What do networks have to do with climate?, Bull. Am. Meteorol. Soc., 87, 585–595, 2006.

Waliser, D. and Guan, B.: Extreme winds and precipitation during landfall of atmospheric rivers, Nat. Geosci., 10, 179–183, https://doi.org/10.1038/ngeo2894, 2017.

Warner, M. D., Mass, C. F., and Salathe Jr, E. P.: Changes in winter atmospheric rivers along the North American west coast in CMIP5 climate models, Journal of Hydrometeorology, 16, 118–128, 2015.

Wolf, F. and Donner, R. V.: Spatial organization of connectivity in functional climate networks describing event synchrony of heavy precipitation, The European Physical Journal Special Topics, pp. 1–19, https://doi.org/0.1140/epjs/s11734-021-00166-1, 2021.

Wolf, F., Bauer, J., Boers, N., and Donner, R. V.: Event synchrony measures for functional climate network analysis : A case study on South American rainfall dynamics, Chaos, 30, 033 102, https://doi.org/10.1063/1.5134012, 2020a.

Wolf, F., Ozturk, U., Cheung, K., and Donner, R. V.: Spatiotemporal patterns of synchronous heavy rainfall events in East Asia during the Baiu season, Earth Syst. Dyn. Discuss., https://esd.copernicus.org/preprints/esd-2020-69/, 2020b.

Xu, G., Ma, X., and Chang, P.: IPART: A Python Package for Image-Processing based Atmospheric River Tracking, Journal of Open Source Software, 5, 2407, https://doi.org/10.21105/joss.02407, 2020.

Yamasaki, K., Gozolchiani, A., and Havlin, S.: Climate networks around the globe are significantly affected by El Niño, Phys. Rev. Lett., 100, 1–4, https://doi.org/10.1103/PhysRevLett.100.228501, 2008.

Zhang, Z., Ralph, F. M., and Zheng, M.: The relationship between extratropical cyclone strength and atmospheric river intensity and position, Geophysical Research Letters, 46, 1814–1823, 2019.

Zhou, Y., O'Brien, T. A., Ullrich, P. A., Collins, W. D., Patricola, C. M., and Rhoades, A. M.: Uncertainties in Atmospheric River Lifecycles by Detection Algorithms: Climatology and Variability, Journal of Geophysical Research: Atmospheres, 126, e2020JD033 711, 2021.

Zhu, Y. and Newell, R. E.: A proposed algorithm for moisture fluxes from atmospheric rivers, Mon. Weather Rev., 126, 725–735, https://doi.org/10.1175/1520-0493(1998)126<0725:APAFMF>2.0.CO;2, 1998.

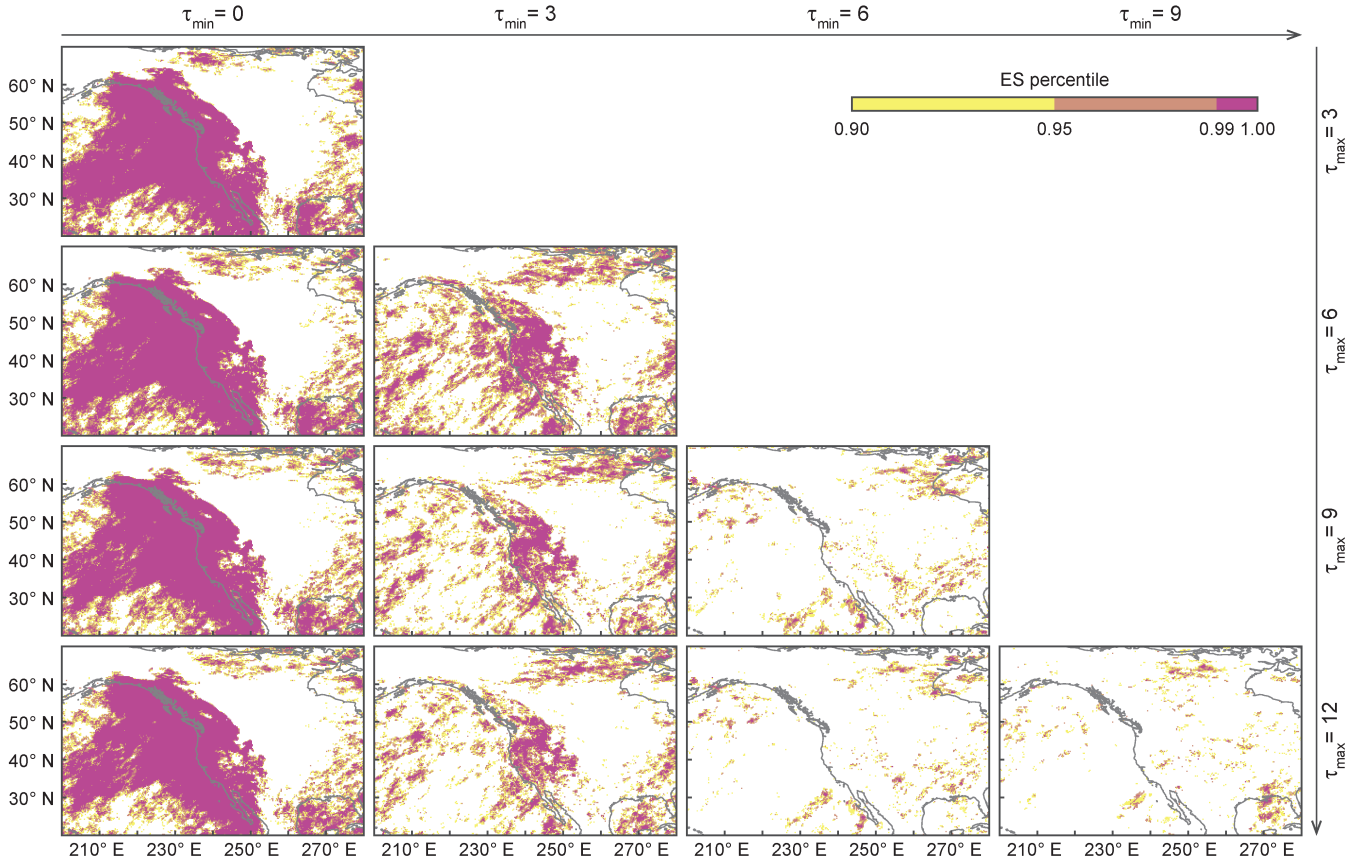

Figure A1. Event synchronization (ES) between ~~time series~~ ARs making landfall on the western coast of ~~heavy rainfall events~~ NA and HPEs. We use the ~~AR time series of the~~ SIO-R1 catalog ~~, considering~~ of land-falling ARs and consider all ARs of ~~category~~ level AR3 ~~and~~ or higher~~that land-fell on the western coast of NA~~. Different values of ~~τ_{min}~~ τ_{min} and ~~τ_{max} were~~ τ_{max} are considered to calculate ES in each panel: ~~τ_{min}~~ τ_{min} increases from left to right and ~~τ_{max}~~ τ_{max} from top to bottom. Color bar as in Fig. ~~??~~2.

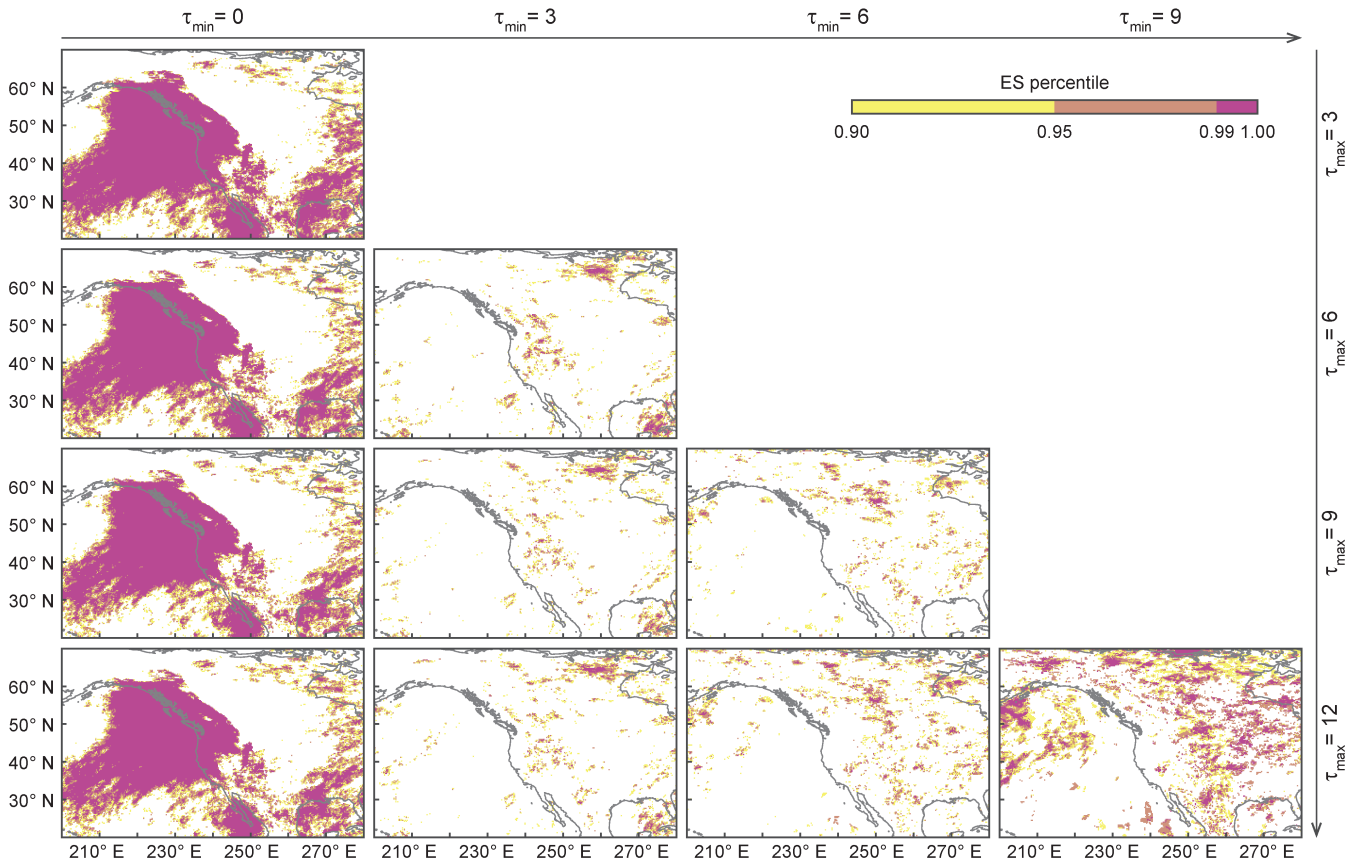

Figure A2. Event synchronization (ES) between ARs making landfall on the western coast of NA and HPEs. We use the IPART catalog of land-falling ARs and consider all ARs of level AR2 or higher. Different values of τ_{min} and τ_{max} were considered to calculate ES in each panel: τ_{min} increases from left to right and τ_{max} from top to bottom. Color bar as in Fig. 2.

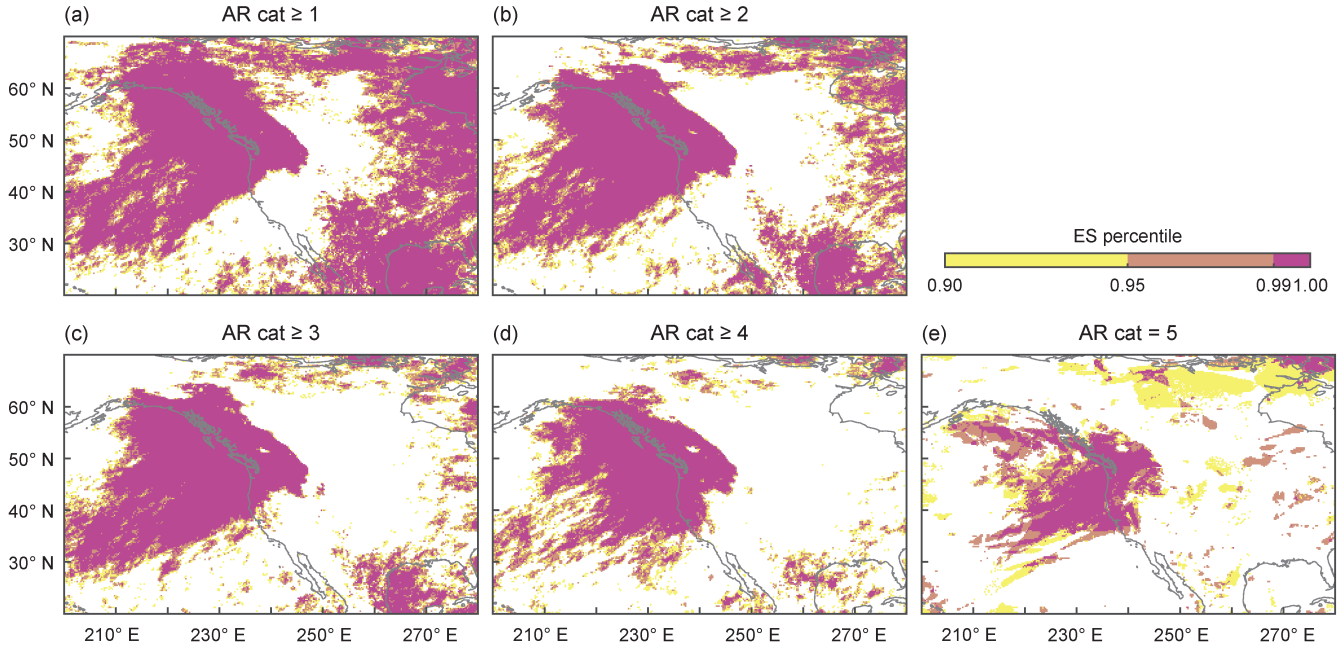

Figure A3. Event synchronization (ES) between ARs making landfall on the western coast of NA and HPEs. We use the SIO-R1 catalog of land-falling ARs but only consider ARs making landfall north of 47.5°N. ES is calculated with $\tau_{\min} = 0$ and $\tau_{\max} = 3$. From (a) to (e) the lower limit of the considered AR level increases: (a) ARs of level AR1 and higher e.g. all ARs, (b) ARs of level AR2 and higher, rest accordingly. Color bar as in Fig. 2.

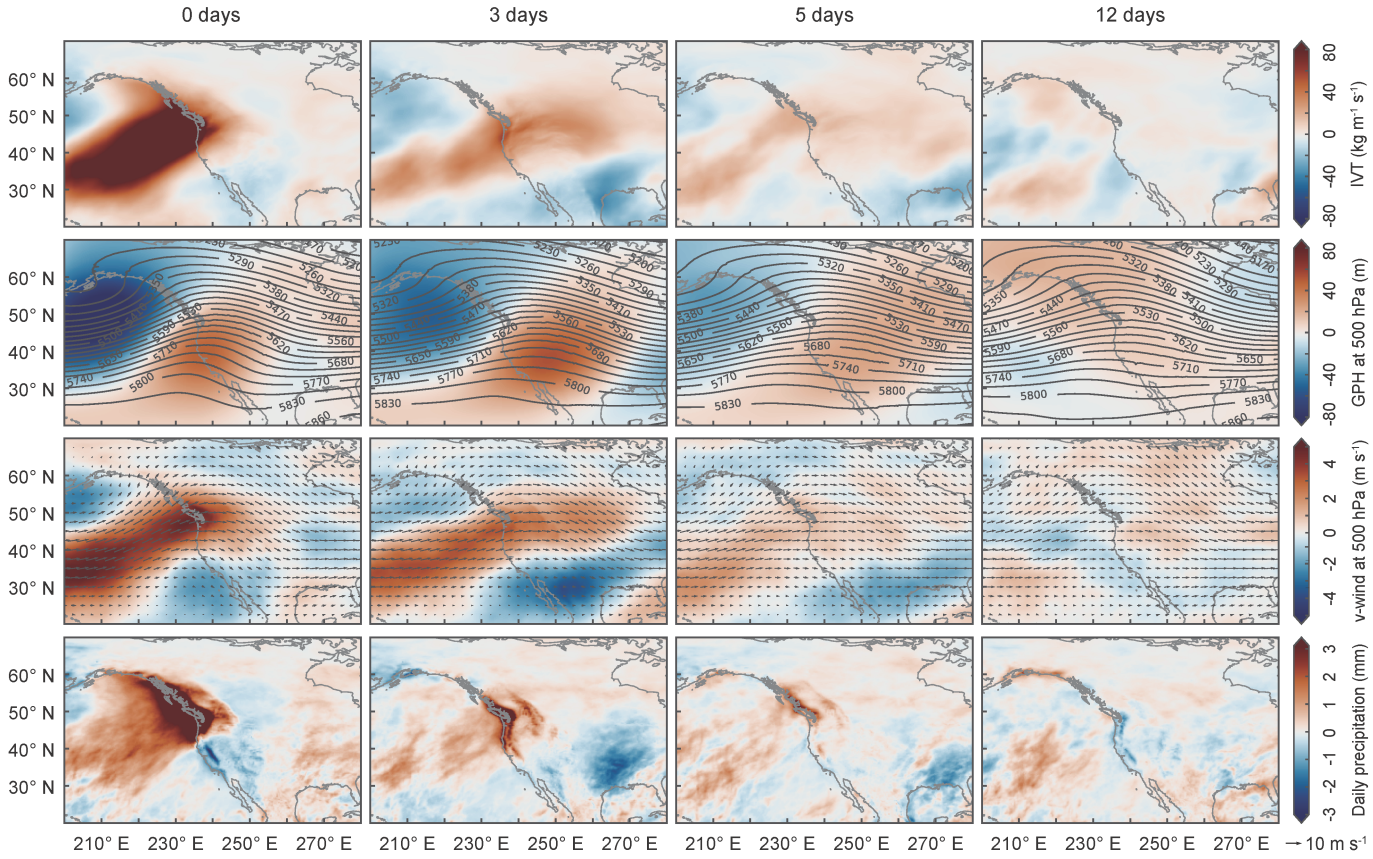

Figure A4. Same as in Fig. 7 but for land-falling ARs that do not synchronize with HPEs in central and eastern Canada.

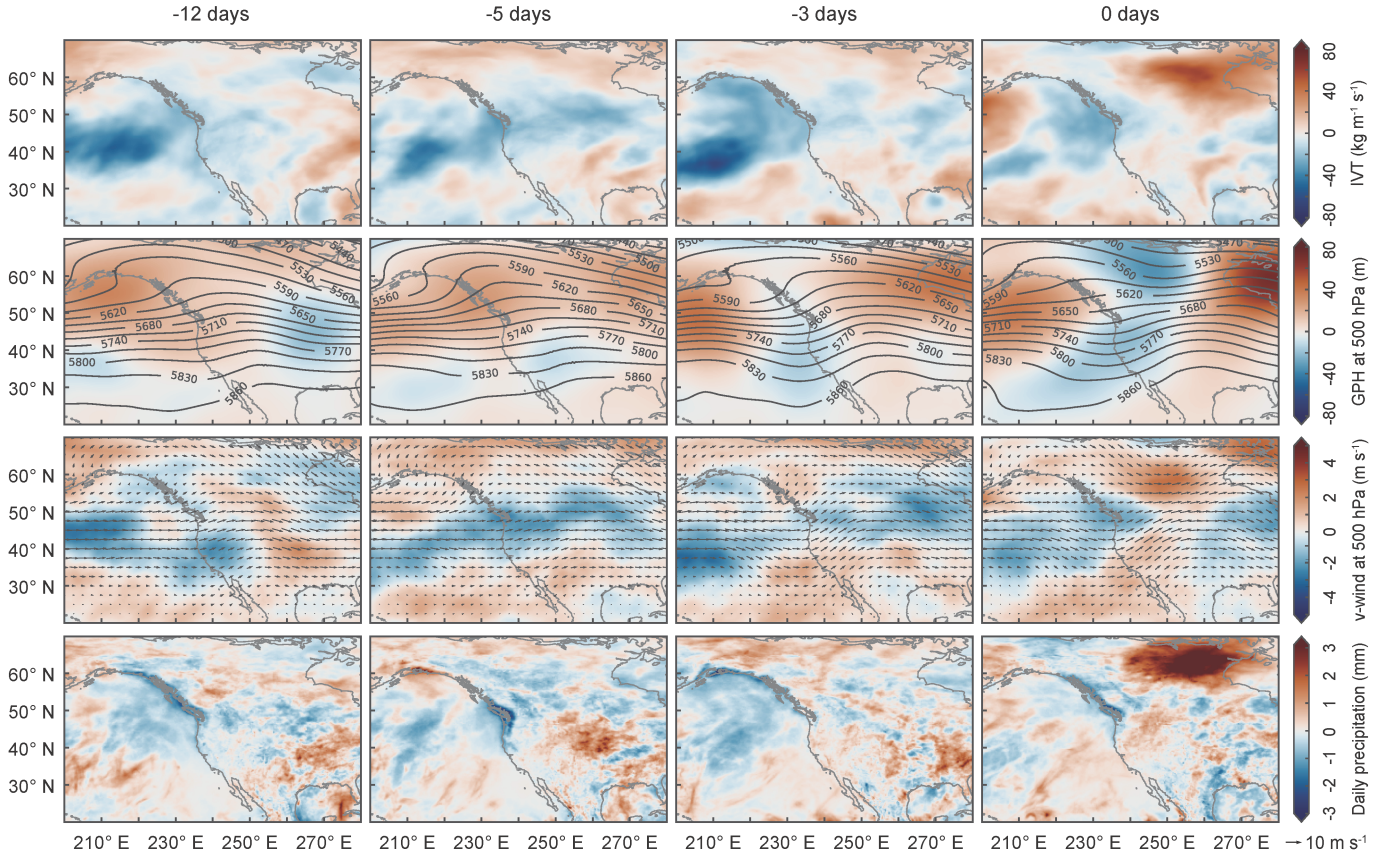

Figure A5. IVT, geopotential height at 500 hPa, wind at 500 hPa, and precipitation anomalies (from top to bottom), from 12, 5, 3, and 0 days (from left to right) before the occurrence of HPEs in central and eastern Canada with no precedent land-falling ARs on the western coast of NA at locations north of 47.5°N, according to the SIO-R1 catalog. Shading, contours and arrows as in Fig. 7

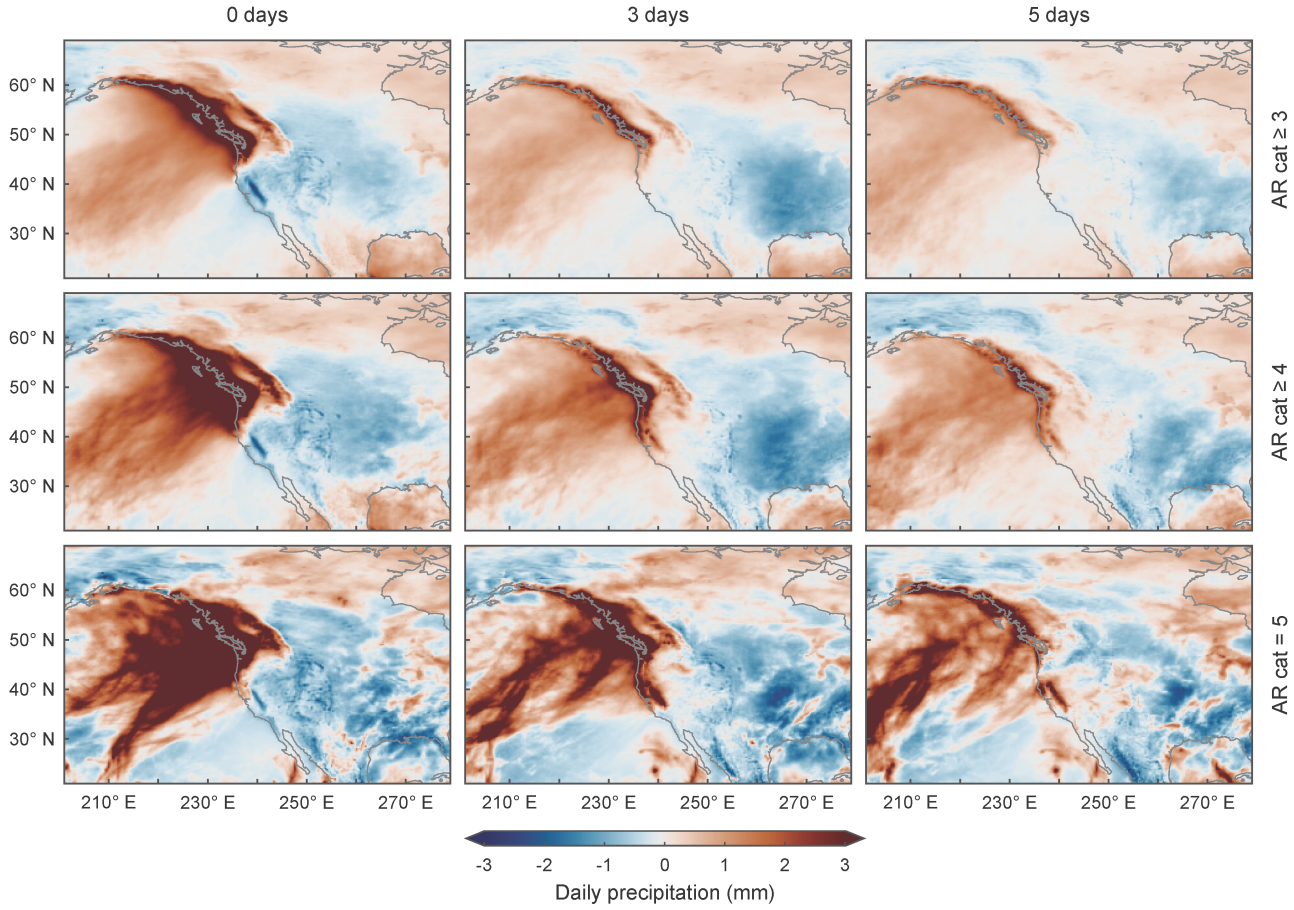

Figure A6. ~~Rainfall~~ Precipitation anomalies, from 0 (left column), 3 (middle column), and 5 (right column) days after the first day of ~~land-falling~~ landfall of an AR of ~~category~~ level AR3 or higher (top row), ~~category~~ level AR4 or higher (middle row), and ~~category~~ level AR5 (bottom row). We only consider ARs land-falling at locations north of $47.5°$N according to the SIO-R1 catalog.